

Alma Mater Studiorum Università di Bologna  
Archivio istituzionale della ricerca

An Experimental Study on Kinetics-Controlled Ca-Carbonate Aqueous Reduction into CH<sub>4</sub> (1 and 2 GPa, 550 degrees C): Implications for C Mobility in Subduction Zones

This is the final peer-reviewed author's accepted manuscript (postprint) of the following publication:

*Published Version:*

An Experimental Study on Kinetics-Controlled Ca-Carbonate Aqueous Reduction into CH<sub>4</sub> (1 and 2 GPa, 550 degrees C): Implications for C Mobility in Subduction Zones / Peng, WG; Tumiati, S; Zhang, LF; Tiraboschi, C; Vitale Brovarone, A; Toffolo, L; Poli, S. - In: JOURNAL OF PETROLOGY. - ISSN 0022-3530. - ELETTRONICO. - 63:8(2022), pp. 1-18. [10.1093/petrology/egac070]

*Availability:*

This version is available at: <https://hdl.handle.net/11585/903836> since: 2023-06-13

*Published:*

DOI: <http://doi.org/10.1093/petrology/egac070>

*Terms of use:*

Some rights reserved. The terms and conditions for the reuse of this version of the manuscript are specified in the publishing policy. For all terms of use and more information see the publisher's website.

This item was downloaded from IRIS Università di Bologna (<https://cris.unibo.it/>).  
When citing, please refer to the published version.

(Article begins on next page)

This is the final peer-reviewed accepted manuscript of:

Peng, WG; Tumiati, S; Zhang, LF; Tiraboschi, C; Vitale Brovarone, A; Toffolo, L; Poli, S: *An Experimental Study on Kinetics-Controlled Ca-Carbonate Aqueous Reduction into CH<sub>4</sub> (1 and 2 GPa, 550 degrees C): Implications for C Mobility in Subduction Zones*

JOURNAL OF PETROLOGY VOL. 63 ISSN 0022-3530

DOI: 10.1093/petrology/egac070

The final published version is available online at:

<https://dx.doi.org/10.1093/petrology/egac070>

Terms of use:

Some rights reserved. The terms and conditions for the reuse of this version of the manuscript are specified in the publishing policy. For all terms of use and more information see the publisher's website.

This item was downloaded from IRIS Università di Bologna (<https://cris.unibo.it/>)

**When citing, please refer to the published version.**

**An experimental study on kinetics-controlled Ca-carbonate aqueous reduction into CH<sub>4</sub> (1 and 2 GPa, 550 °C): Implications for C mobility in subduction zones**

Weigang Peng<sup>1,2,3\*</sup>, Simone Tumiati<sup>2</sup>, Lifei Zhang<sup>3</sup>, Carla Tiraboschi<sup>4</sup>, Alberto Vitale Brovarone<sup>5,6,7</sup>, Luca Toffolo<sup>2</sup> and Stefano Poli<sup>2</sup>

<sup>1</sup>College of Oceanography, Hohai University, Nanjing 210098, China

<sup>2</sup>Dipartimento di Scienze della Terra, Università degli Studi di Milano, via Mangiagalli 34, 20133 Milano, Italy

<sup>3</sup>MOE Key Laboratory of Orogenic Belts and Crustal Evolution, School of Earth and Space Sciences, Peking University, Beijing 100871, China

<sup>4</sup>Institut für Mineralogie, Universität Münster, Corrensstrasse 24, 48149 Münster, Germany

<sup>5</sup>Dipartimento di Scienze Biologiche, Geologiche e Ambientali, Alma Mater Studiorum Università di Bologna, Piazza di Porta San Donato 1, 40126 Bologna, Italy

<sup>6</sup>Sorbonne Université, Muséum National d'Histoire Naturelle, UMR CNRS 7590, IRD, Institut de Minéralogie, de Physique des Matériaux et de Cosmochimie, IMPMC, 75005 Paris, France

<sup>7</sup>Institute of Geosciences and Earth Resources, National Research Council of Italy, via G. Moruzzi 1, 56124 Pisa, Italy

\* Corresponding author: Weigang Peng (weigang.peng1992@gmail.com)

Running Title: Abiotic CH<sub>4</sub> generation in subduction zones

© The Author(s) 2022. Published by Oxford University Press. All rights reserved.

For Permissions, please email: journals.permissions@oup.com

## ABSTRACT

Abiotic methane ( $\text{CH}_4$ ) generation under subduction zone conditions has been experimentally investigated through aqueous reduction of pure C-bearing materials (e.g. carbonate minerals and organic matter). However, quantitative assessments of  $\text{CH}_4$  production in these experiments, as well as the potential effects of other components such as silica (Si) on the reduction processes, have not yet been well established. Here, we performed experiments to quantitatively evaluate the time-resolved Ca-carbonate aqueous reduction into  $\text{CH}_4$  at  $P = 1$  and 2 GPa, and  $T = 550$  °C in the  $\text{CaO} + \text{COH}$ ,  $\text{CaO} + \text{SiO}_2 + \text{COH}$ , and  $\text{CaO} + \text{SiO}_2 + \text{MgO} + \text{COH}$  systems, employing calcite + water  $\pm$  quartz  $\pm$  serpentine (synthetic chlorine (Cl)-bearing chrysotile and natural Fe–Al-bearing antigorite) as starting materials. Redox conditions of the experiments were buffered by iron–wüstite (IW) using a double capsule setting, corresponding to oxygen fugacity ( $f\text{O}_2$ ) values (expressed as log units relative to the fayalite–magnetite–quartz buffer,  $\Delta\text{FMQ}$ ) in the inner capsule of  $\Delta\text{FMQ} \approx -5.5$  at 1 GPa and  $\Delta\text{FMQ} \approx -6.0$  at 2 GPa. The solid products are mainly composed of portlandite  $\pm$  larnite  $\pm$  wollastonite  $\pm$  brucite, while Ca-carbonate and/or silicate reactants commonly occur as relicts. Quadrupole mass spectrometric analysis shows that  $\text{CH}_4$  and  $\text{H}_2\text{O}$  are the major COH molecular species in the fluid products, with molar ratios between  $\text{CH}_4$  and starting calcite representing the reaction progress ranging from  $\sim 0.13$  to  $\sim 1.00$ . Comparisons of

experimental run products with thermodynamically predicted phase assemblages, together with time-series experiments, indicate that the reduction processes are primarily controlled by reaction kinetics. At 1 GPa and 550 °C, rate constants of  $4.0 \times 10^{-6} \text{ s}^{-1}$ ,  $7.4 \times 10^{-6} \text{ s}^{-1}$ , and  $2.6 \times 10^{-6} \text{ s}^{-1}$  were retrieved for reactions starting with calcite + quartz + water, calcite + synthetic Cl-bearing chrysotile + water, and calcite + natural Fe–Al-bearing antigorite + water, respectively, significantly higher than the constant of  $0.8 \times 10^{-6} \text{ s}^{-1}$  for the silicate-absent reaction. Besides, an increase in pressures can also enhance the reduction efficiency of Ca-carbonates until reaching equilibrium with the fluids. Our data provide experimental evidence for kinetics-controlled Ca-carbonate aqueous reduction into  $\text{CH}_4$  in subduction zones, indicating that silicate involvement and/or pressure increase can accelerate the reaction rates through short-lived fluid–rock interactions, which may have important implications for deep C mobility.

**Key words:** abiotic  $\text{CH}_4$ ; Ca-carbonate aqueous reduction; deep C mobility; experimental petrology; reaction kinetics

## INTRODUCTION

Investigating the geological production of  $\text{CH}_4$  may be essential for deciphering the chemolithoautotrophic origin of life on Earth and other planetary bodies in our

solar system (e.g. Kelley *et al.*, 2005; Russell *et al.*, 2010; McCollom & Seewald, 2013; Plümper *et al.*, 2017; Klein *et al.*, 2019; Ménez, 2020; Truche *et al.*, 2020; Vitale Brovarone *et al.*, 2020). The generation of CH<sub>4</sub> on Earth can be attributed to either biotic or abiotic processes. Biotic CH<sub>4</sub> is widely distributed in surface environments, originating primarily from microbial processes or thermogenic degradation of organic matter. Abiotic CH<sub>4</sub>, formed by chemical reactions that are independent from biotic processes, has been recognized over a wide range of geological contexts particularly in submarine serpentinite-hosted hydrothermal fields and Precambrian crystalline shields (see Etiope & Sherwood Lollar, 2013 and Etiope & Schoell, 2014 for reviews). Furthermore, an increasing number of field and experimental studies have been conducted on abiotic CH<sub>4</sub> generation under subduction zone conditions, offering potential insights into the mechanisms of deep C mobility (Scott *et al.*, 2004; Shi *et al.*, 2005; Sachan *et al.*, 2007; Sharma *et al.*, 2009; Song *et al.*, 2009; Arai *et al.*, 2012; Lazar *et al.*, 2014; Huang *et al.*, 2017; Li, 2017; Mukhina *et al.*, 2017; Vitale Brovarone *et al.*, 2017, 2020; Tao *et al.*, 2018; Giuntoli *et al.*, 2020; Boutier *et al.*, 2021; Peña-Alvarez *et al.*, 2021; Peng *et al.*, 2021; Zhang *et al.*, 2021; Spránitz *et al.*, 2022).

Redox states in subduction zones, described using variables like  $fO_2$ ,  $\mu O_2$  ( $O_2$  chemical potential), or  $nO_2$  ( $O_2$  molar quantity) (Tumiati *et al.*, 2015), modulate the valence and speciation of subducted C such as carbonate minerals, CO<sub>2</sub>,

graphite/diamond, and CH<sub>4</sub> (e.g. Hayes & Waldbauer, 2006; Evans, 2012; Galvez & Pubellier, 2019; Tumiati & Malaspina, 2019; Sheik *et al.*, 2020). At relatively oxidized conditions where C<sup>4+</sup> is stable, interactions between COH fluids and several slab- and mantle wedge-derived lithologies at forearc to subarc depths commonly generate carbonate minerals, contributing to C sequestration in subduction zones (e.g. Tumiati *et al.*, 2013; Piccoli *et al.*, 2016, 2018, 2021; Scambelluri *et al.*, 2016; Jaeckel *et al.*, 2018; Sieber *et al.*, 2018, 2020, 2022; Consuma *et al.*, 2020; Peng *et al.*, 2020; Hu *et al.*, 2021; Okamoto *et al.*, 2021). Conversely, reduced C including hydrocarbons (e.g. CH<sub>4</sub>) and graphite would progressively become dominant C-bearing species imposed by decreasing  $fO_2$  at convergent margins, as suggested by both rock-based investigations and experimental simulations (see below). Subduction-related production of CH<sub>4</sub> has been recorded in ophicalcites from the Italian Western Alps, ascribed to calcite methanation induced by H<sub>2</sub>-riched fluids at  $\Delta FMQ$  -6.0 to -3.0 at 1.0–2.0 GPa and 400–500 °C (Vitale Brovarone *et al.*, 2017; Giuntoli *et al.*, 2020). Besides, CH<sub>4</sub>-bearing fluid inclusions were reported in carbonated eclogites from the Chinese southwestern Tianshan, which, combined with experimental studies, demonstrates aqueous reduction of Fe-bearing dolomite at  $\Delta FMQ$  -2.5 to -1.5 at 2.5–3.0 GPa and 500–575 °C (Tao *et al.*, 2018). Further, abiogenic CH<sub>4</sub> generation in exhumed ophidolomites from the Chinese southwestern Tianshan has underscored the

potential role of hydrogen fugacity ( $f_{H_2}$ ) in carbonate reduction in subduction zones, elucidating that an infiltration of  $H_2O$ -rich fluids characterized by relatively high  $f_{H_2}$  can result in dolomite transformation into  $CH_4$  starting at 0.7–0.9 GPa and 410–430 °C (Peng *et al.*, 2021). In addition to carbonate-bearing lithologies, abiotic  $CH_4$  has also been observed in several slab- and mantle wedge-derived partially serpentinized rocks, as well as orogenic peridotites, interpreted as resulting from reduction of C-bearing species in metamorphic fluids through subduction zone serpentinization (Sachan *et al.*, 2007; Vitale Brovarone *et al.*, 2020; Boutier *et al.*, 2021; Zhang *et al.*, 2021). Experiments conducted at 1.5–2.5 GPa and 600–700 °C (Li, 2017) and 2.4–3.5 GPa and 300 °C (Huang *et al.*, 2017) suggest that aqueous reduction of carboxylic acids or carboxylates represents a potential pathway leading to the formation of  $CH_4$  (commonly with other short-chain hydrocarbons) in subduction zones. Moreover, several experiments have evaluated the important role of low  $f_{O_2}$  far below the FMQ buffer in high-pressure (HP) Ca-carbonate aqueous reduction into  $CH_4$  (see below). Experiments performed by Lazar *et al.* (2014) in the  $CaO + COH$  system at 0.2–1.0 GPa and 300–700 °C indicate that low  $f_{O_2}$  values buffered by iron–magnetite (IM) or wüstite–magnetite (WM) are favorable for the reduction of subducted calcite into  $CH_4$ . Similar conclusions were reached by Mukhina *et al.* (2017) who observed high yields of hydrocarbons (mostly  $CH_4$ ) in the  $CaO + Fe/FeO + COH$  system buffered by iron or IW at

2.0–6.6 GPa and 400–600 °C. The reported experiments mainly qualitatively evaluated the effects of  $P$ – $T$ – $fO_2$  conditions on abiotic  $CH_4$  generation through aqueous reduction of pure C-bearing materials. However, little attention has been paid to the quantification of  $CH_4$  in such reduction experiments that are dependent on run durations (Barbier *et al.*, 2020 and references therein). Experiments have suggested that the dissolved  $SiO_2$  in subduction zone aqueous fluids may induce partial dissolution of graphite by synthesizing organic complexes, thereby contributing to elevated  $CO_2$  concentrations in the fluids (Tumiati *et al.*, 2017, 2020). Nevertheless, it remains undetermined whether  $SiO_2$ , a key component comprising lithospheric rocks mainly in the form of silicates, can influence Ca-carbonate aqueous reduction and thus  $CH_4$  production under subduction zone conditions.

In this contribution, we experimentally investigated kinetics-controlled abiotic  $CH_4$  formation through Ca-carbonate aqueous reduction in the  $CaO + COH$ ,  $CaO + SiO_2 + COH$ , and  $CaO + SiO_2 + MgO + COH$  systems buffered by IW both at 1 and 2 GPa at 550 °C (24–264 h), using calcite + water  $\pm$  quartz  $\pm$  serpentine (synthetic Cl-bearing chrysotile (hereafter referred to as synthetic chrysotile) and natural Fe–Al-bearing antigorite (hereafter referred to as natural antigorite)) as starting materials. Experimental and modelling results of solid and fluid products, as well as calculations for reaction rates, are shown and discussed to improve our

comprehension of the kinetics-controlled reduction processes in subduction zones. For comparison, dry and/or wet experiments starting with calcite, quartz, synthetic chrysotile, and natural antigorite separately were performed under the same  $P$ - $T$ - $fO_2$  conditions, to investigate whether  $CH_4$  can be produced by dry reduction of Ca-carbonates and to evaluate whether the silicate reactants were hosts for C-bearing materials representing the potential contaminants. Chemical formulas and abbreviations of phases in this study are listed in Table 1.

## **EXPERIMENTAL METHODS**

### **Experimental conditions and apparatus**

Experiments were performed with an end-loaded piston-cylinder apparatus at  $P = 1$  and 2 GPa, and  $T = 550$  °C in the Experimental Petrology Laboratory of the Department of Earth Sciences, University of Milan (Italy). Pressure calibration of the piston-cylinder apparatus is based on the quartz-coesite transition (Bose & Ganguly, 1995) at 2.93 GPa and 800 °C, and 3.07 GPa and 1000 °C, resulting in an accuracy of  $\pm 0.01$  GPa. Temperatures were measured using a K-type thermocouple with an accuracy of  $\pm 5$  °C. Samples were first pressurized at the run pressures and then heated to 550 °C, with a ramp of  $\sim 100$  °C/min. Experiments were quenched by turning off the power supply, leading to a high rate of temperature decrease of  $> 40$  °C/s, and thus compositions of the quenched COH fluids as well as solid phases

(see below) are considered to represent those at the experimental  $P$ – $T$  conditions (e.g. Matveev *et al.*, 1997; Tiraboschi *et al.*, 2022). After quenching, capsules (see below) were recovered and cleaned with hydrochloric acid. The outer capsule was peeled off, exposing the inner capsule, and dried in a vacuum oven at 110 °C (> 2 h) to eliminate the residual water trapped in the oxygen buffer (Tiraboschi *et al.*, 2016; Tumiati *et al.*, 2020).

### **Starting materials and buffering strategy**

The conventional double capsule technique (Eugster & Skippen, 1967) was employed to constrain  $fH_2$  conditions (and, indirectly, redox states) of the experiments and to prevent the direct contact of starting materials with the IW buffer. Starting materials were loaded in an inner Au<sub>60</sub>Pd<sub>40</sub> capsule (OD = 2.3 mm), which was placed in an outer Au capsule (OD = 4.5 mm) containing the buffering assemblage. Reagent-grade pure calcite powder (Sigma-Aldrich), natural hyaline quartz powder, synthetic chrysotile containing ~1 wt% Cl (provided by Marcello Campione, University of Milan-Bicocca; Villa *et al.*, 2018), natural antigorite containing ~4 wt% FeO and ~2 wt% Al<sub>2</sub>O<sub>3</sub> from the Western Alps (provided by Chiara Groppo, University of Turin; Vitale Brovarone *et al.*, 2017), and ultrapure Milli-Q water were used as starting materials. In experiments starting with a single kind of mineral with or without added water, the solid reactant (calcite, quartz,

synthetic chrysotile, or natural antigorite) was evenly distributed in the inner capsule (e.g. calcite + water in Fig. 1a). By contrast, in experiments starting with calcite and another mineral (quartz, synthetic chrysotile, or natural antigorite) with added water, solid reactants were layered in the inner capsule (Fig. 1b and c). At relatively short run durations in this study, the layered starting materials allowed the preservation of chemical gradients in the inner capsule, so that the fluid products could coexist with a variety of solid phases, even if metastable, to investigate their effects on the kinetics of Ca-carbonate aqueous reduction into CH<sub>4</sub> (see Section *Discussion*). The double capsule was embedded in a sintered MgO rod (Norton Ceramics), surrounded by a graphite heater and a NaCl sleeve. A pyrophyllite-steel plug was placed at the top of the assembly to ensure electrical contact. Since the Au<sub>60</sub>Pd<sub>40</sub> alloy of the inner capsule is permeable to H<sub>2</sub>,  $fH_2$  conditions in the inner capsule are expected to be the same as those in the outer capsule (Tiraboschi *et al.*, 2016, 2018; Tumiati *et al.*, 2017, 2020). The starting IM buffer (with added excess water) has always been converted into the IW buffer during experimental runs (Fig. 1d), which remains stable at the studied  $P$ - $T$  conditions (Fig. 1e; e.g. Eugster & Wones, 1962; Jenkins & Bozhilov, 2003). Thus, the IW buffer constrained  $fH_2$  values in both inner and outer capsules by the following reaction throughout the runs, as reflected by the preservation of all the buffering phases after quenching (Fig. 1d):



Since  $f\text{O}_2$  conditions in the inner and outer capsules are identical only when both of them contain pure water (Eugster & Skippen, 1967),  $f\text{O}_2$  values in the inner capsule are expected to be slightly lower than  $f\text{O}_2^{\text{IW}}$  (Luth, 1989; Tumiati *et al.*, 2017, 2020; Miozzi & Tumiati, 2020) in our experiments where fluids are nearly binary mixtures of  $\text{CH}_4$  and  $\text{H}_2\text{O}$  (Table 2).

## **ANALYTICAL TECHNIQUES**

### **Analysis of solids**

Chemical analysis, back-scattered electron imaging, and element mapping of the solid products were conducted using a JEOL 8200 wavelength-dispersive electron microprobe at the Department of Earth Sciences, University of Milan (Italy). The running conditions were 15 kV acceleration voltage and 5 nA beam current, with a beam diameter of  $\sim 1 \mu\text{m}$ . The adopted mineral standards were grossular (Si, Al, and Ca), ilmenite (Ti), pure Cr (Cr), fayalite (Fe), rhodonite (Mn), olivine (Mg), and orthoclase (K). A counting time of 30 s (10 s background) was applied for all the elements. The PRZ correction was performed at the final calibration stage.

### **Analysis of fluid species**

To measure COH molecular species in the fluid products, we employed the capsule-piercing technique (Tiraboschi *et al.*, 2016; see also Tiraboschi *et al.*, 2022 for a review with respect to the quantification of COH fluids through *ex situ* experiments) at the Department of Earth Sciences, University of Milan (Italy). After quenching, fluids were extracted from the inner capsule in a Teflon extraction vessel (reactor), which was heated by an electric furnace to ~90 °C to convert liquid water into water vapor. Then, fluids were conveyed into a quadrupole mass spectrometer (QMS) using ultrapure argon (Ar) as the carrier gas. The QMS was connected to the reactor by a heated line (~90 °C) to avoid water vapor condensation on metal tubes. Pressures in the reactor were measured by a high-resolution sensor gauge, with an accuracy of  $\pm 1$  mbar. Temperatures in the reactor were monitored by a K-type thermocouple. The internal volume of the reactor was constrained based on the distance between its base and top parts. Thus, the total moles of gases ( $n$ ) released from the inner capsule were retrieved using the ideal gas law  $n = \Delta P * V / (R * T)$ , where  $\Delta P$  is the pressure increase in the reactor after piercing,  $V$  is the volume of the reactor,  $R$  is the gas constant, and  $T$  is the temperature in the reactor during piercing.

During the QMS analysis, selected mass/charge ( $m/z$ ) channels were monitored to measure the COH fluid species. The QMS calibration was performed using double-distilled water (typically 1  $\mu$ L) and three gas mixtures with known

compositions (80 vol% Ar + 10 vol% CO<sub>2</sub> + 10 vol% O<sub>2</sub>, 80 vol% Ar + 10 vol% CH<sub>4</sub> + 10 vol% CO, and 90 vol% Ar + 10 vol% H<sub>2</sub>). The calibration enables the retrieval of micromoles (μmol) of H<sub>2</sub>O, CH<sub>4</sub>, CO<sub>2</sub>, CO, H<sub>2</sub>, and O<sub>2</sub>, with uncertainties of ~1 mol% for all the species except for CO (~10 mol%) due to the interference of atmospheric N<sub>2</sub> on the 28 *m/z* channel (Tumiati *et al.*, 2020). When the fluid products were transferred into the QMS, micromolar concentrations of COH molecular species were obtained by comparing the integrated fragmentation peaks of characteristic *m/z* channels (e.g. channels 15, 14, 12, and 2 for CH<sub>4</sub>; see Supplementary Data Fig. S1 for a representative channel 15 in runs COH115 and COH116) with those of the calibration gases, taking into account all possible interferences using a least squares regression method (Tiraboschi *et al.*, 2016). Monte Carlo simulations provided the propagation of uncertainties for the COH fluid species, corresponding to their measurement uncertainties. Further, the measured concentrations of COH molecular species, as well as their uncertainties, were recalculated based on the total amounts of fluids retrieved using the ideal gas law (see above).

## EXPERIMENTAL RESULTS

Representative mineral compositions of the solid products in selected runs are listed in Supplementary Data Table S1, and concentrations of COH molecular

species in the fluid products are shown in Table 2 & Supplementary Data Table S2. Experiments employing calcite and water as starting materials, with or without the addition of quartz, synthetic chrysotile, or natural antigorite, are always characterized by significant production of CH<sub>4</sub>-bearing aqueous fluids, showing molar ratios between CH<sub>4</sub> and starting calcite (CH<sub>4</sub>/Cal<sub>molar</sub>) representing the completeness of reactions ranging from ~0.13 to ~1.00 (Fig. 2; Table 2). Conversely, C-bearing species are nearly absent in comparative experiments starting with dry calcite, quartz ± water, dry synthetic chrysotile, and dry natural antigorite separately (Supplementary Data Table S2). At run conditions, residual Ca-carbonates occur in the form of calcite (1 GPa) and aragonite (2 GPa) as identified by Raman Spectroscopy (Supplementary Data Fig. S2; see Tumiaty *et al.*, 2020 for detailed methods). Graphite is never observed in the run products.

### **System CaO + COH**

Experiments starting with calcite + water both at 1 and 2 GPa at 550 °C (24–240 h) are characterized by the growth of portlandite crystals at the expense of Ca-carbonate grains (Fig. 3 & Supplementary Data Fig. S3). In experiments for 72 h, the total amounts of fluids are 49.25 μmol at 1 GPa (run COH115) and 83.81 μmol at 2 GPa (run COH116), in which H<sub>2</sub>O and CH<sub>4</sub> are the major components whereas CO<sub>2</sub> and CO occur in minor amounts (Table 2). In run COH115, the concentrations

of H<sub>2</sub>O and CH<sub>4</sub> are  $33.77 \pm 0.09$   $\mu\text{mol}$  ( $68.6 \pm 0.2$  mol%) and  $13.9 \pm 0.1$   $\mu\text{mol}$  ( $28.2 \pm 0.2$  mol%), respectively, with  $X_{\text{CH}_4}$  ( $=\text{CH}_4/(\text{CH}_4 + \text{H}_2\text{O})_{\text{molar}}$ ) of  $0.292 \pm 0.002$  (Table 2). The recovered fluids in run COH116 contain  $56.2 \pm 0.2$   $\mu\text{mol}$  ( $68.1 \pm 0.2$  mol%) H<sub>2</sub>O and  $23.7 \pm 0.2$   $\mu\text{mol}$  ( $28.7 \pm 0.3$  mol%) CH<sub>4</sub>, with  $X_{\text{CH}_4}$  of  $0.297 \pm 0.002$  (Table 2). The CH<sub>4</sub>/Cal<sub>molar</sub> ratio at 2 GPa ( $0.624 \pm 0.005$ ) is about twice that at 1 GPa ( $0.331 \pm 0.002$ ), and the molar ratio between the generated total C-bearing species (including CH<sub>4</sub>, CO<sub>2</sub>, and CO) and starting calcite ( $C_{\text{tot}}/\text{Cal}_{\text{molar}}$ ) at 2 GPa ( $0.69 \pm 0.05$ ) is considerably higher than that at 1 GPa ( $0.37 \pm 0.02$ ) (Fig. 2; Table 2).

To evaluate the effects of run durations, replicated experiments were performed for 24 h (run COH193) and 240 h (run COH194) at 1 GPa and 550 °C. The portlandite selvage width in run COH194 (Fig. 3d–f) is larger than that in run COH193 (Fig. 3a–c). The total amounts of fluids are 11.62  $\mu\text{mol}$  in run COH193 and 27.29  $\mu\text{mol}$  in run COH194, in which H<sub>2</sub>O and CH<sub>4</sub> are generally dominant (Table 2). In run COH193, the concentrations of H<sub>2</sub>O and CH<sub>4</sub> are  $4.3 \pm 0.2$   $\mu\text{mol}$  ( $39 \pm 2$  mol%) and  $5.5 \pm 0.1$   $\mu\text{mol}$  ( $51 \pm 1$  mol%), respectively, with  $X_{\text{CH}_4}$  of  $0.56 \pm 0.02$  (Table 2). The recovered fluids in run COH194 contain  $3.4 \pm 0.2$   $\mu\text{mol}$  ( $12.3 \pm 0.7$  mol%) H<sub>2</sub>O and  $17.4 \pm 0.1$   $\mu\text{mol}$  ( $63.6 \pm 0.5$  mol%) CH<sub>4</sub>, with  $X_{\text{CH}_4}$  of  $0.838 \pm 0.009$  (Table 2). Compared with the 3-day-long run COH115, the 1-day-long run COH193 has lower CH<sub>4</sub>/Cal<sub>molar</sub> and  $C_{\text{tot}}/\text{Cal}_{\text{molar}}$  ratios of  $0.131 \pm 0.003$  and  $0.16 \pm$

0.04, respectively, while the 10-day-long run COH194 has higher ratios of  $0.413 \pm 0.003$  and  $0.57 \pm 0.05$ , respectively (Fig. 2; Table 2).

### **System CaO + SiO<sub>2</sub> + COH**

Experiments starting with layered calcite + quartz + water both at 1 and 2 GPa at 550 °C (72 h) produced similar mineral assemblages mainly composed of portlandite, larnite, wollastonite, as well as residual Ca-carbonates and quartz. Larnite commonly forms a coronitic layer between portlandite and wollastonite, which in turn replace Ca-carbonates and quartz, respectively (Fig. 4). The solid products are characterized by relatively loosely packed mineral grains filled with pores, representing connected fluid pathways throughout the inner capsule (Fig. 4). The total amounts of fluids in these experiments are 44.20 μmol at 1 GPa (run COH200) and 55.60 μmol at 2 GPa (run COH125), which consist mainly of H<sub>2</sub>O and CH<sub>4</sub> while CO<sub>2</sub> and CO occur as minor species (Table 2). In run COH200, the concentrations of H<sub>2</sub>O and CH<sub>4</sub> are  $23.15 \pm 0.04$  μmol ( $56.0 \pm 0.1$  mol%) and  $16.78 \pm 0.03$  μmol ( $40.60 \pm 0.07$  mol%), respectively, with  $X_{\text{CH}_4}$  of  $0.420 \pm 0.001$  (Table 2). The recovered fluids in run COH125 contain  $31.79 \pm 0.06$  μmol ( $60.9 \pm 0.1$  mol%) H<sub>2</sub>O and  $17.24 \pm 0.07$  μmol ( $33.0 \pm 0.1$  mol%) CH<sub>4</sub>, with  $X_{\text{CH}_4}$  of  $0.352 \pm 0.001$  (Table 2). The  $\text{CH}_4/\text{Ca}_{\text{molar}}$  and  $\text{C}_{\text{tot}}/\text{Ca}_{\text{molar}}$  ratios at 2 GPa ( $0.663 \pm 0.003$

and  $0.78 \pm 0.03$ , respectively) are slightly higher than those at 1 GPa ( $0.645 \pm 0.001$  and  $0.70 \pm 0.02$ , respectively) (Fig. 2; Table 2).

### **System CaO + SiO<sub>2</sub> + MgO + COH (synthetic Cl-bearing chrysotile)**

Experiments starting with layered calcite + synthetic chrysotile (containing ~1 wt% Cl) + water both at 1 and 2 GPa at 550 °C (72–264 h) generated similar solid products of mainly portlandite, larnite, and brucite (Fig. 5). At 1 GPa, portlandite and larnite grow by replacing Ca-carbonate grains, with calcite relicts and larnite-hosted merwinite inclusions occasionally visible (Fig. 5a and b). At 2 GPa, by contrast, aragonite is never observed in the products (Fig. 5d–f). In these experiments, starting chrysotile has been completely consumed by newly formed phases (Fig. 5). The total amounts of fluids at 1 GPa are 58.10 μmol in run COH201 (72 h) and 39.83 μmol in run COH146 (240 h), containing mainly H<sub>2</sub>O and CH<sub>4</sub> as well as minor amounts of CO<sub>2</sub> and CO (Table 2). In run COH201, the concentrations of H<sub>2</sub>O and CH<sub>4</sub> are  $33.8 \pm 0.1$  μmol ( $62.0 \pm 0.2$  mol%) and  $20.46 \pm 0.09$  μmol ( $37.6 \pm 0.2$  mol%), respectively, with  $X_{\text{CH}_4}$  of  $0.377 \pm 0.002$  (Table 2). In run COH146, by contrast, the concentration of H<sub>2</sub>O decreases to  $14.4 \pm 0.3$  μmol ( $37.4 \pm 0.7$  mol%) while that of CH<sub>4</sub> increases to  $24.0 \pm 0.2$  μmol ( $62.2 \pm 0.6$  mol%), with  $X_{\text{CH}_4}$  of  $0.625 \pm 0.007$  (Table 2). The  $\text{CH}_4/\text{Cal}_{\text{molar}}$  and  $\text{C}_{\text{tot}}/\text{Cal}_{\text{molar}}$  ratios in the 3-day-long run COH201 are  $0.853 \pm 0.004$  and  $0.89 \pm 0.03$ ,

respectively, while those in the 10-day-long run COH146 are very close to 1 (Fig. 2; Table 2). Although fluid components at 2 GPa for 264 h (run COH147) show lower absolute concentrations ( $\mu\text{mol}$ ) than those in runs COH201 and COH146, likely imputable to the partial fluid loss, their relative concentrations (mol%) are generally comparable (Table 2). In run COH147, the relative concentrations of  $\text{H}_2\text{O}$  and  $\text{CH}_4$  are  $32.9 \pm 0.7$  mol% and  $66.4 \pm 0.6$  mol%, respectively, with  $X_{\text{CH}_4}$  of  $0.668 \pm 0.007$  (Table 2).

#### **System $\text{CaO} + \text{SiO}_2 + \text{MgO} + \text{COH}$ (natural Fe–Al-bearing antigorite)**

Experiments starting with layered calcite + natural antigorite (containing ~4 wt% FeO and ~2 wt%  $\text{Al}_2\text{O}_3$ ) + water resulted in the formation of portlandite, larnite, and brucite, together with monticellite and forsterite-rich olivine at 1 GPa and 550 °C for 72 h (Fig. 6a–c) and merwinite at 2 GPa and 550 °C for 96 h (Fig. 6d and e). Besides, Al-bearing minerals such as chlorite and vesuvianite occur in the solid products (Fig. 6c and e). In these experiments, Ca-carbonate relicts are commonly observed (Fig. 6a and d), whereas starting antigorite has been completely exhausted. The recovered fluids, with total amounts of 59.36  $\mu\text{mol}$  at 1 GPa (run COH119) and 85.77  $\mu\text{mol}$  at 2 GPa (run COH126), are mainly composed of  $\text{H}_2\text{O}$  and  $\text{CH}_4$  while the concentrations of  $\text{CO}_2$  and CO are relatively low (Table 2). In run COH119, the concentrations of  $\text{H}_2\text{O}$  and  $\text{CH}_4$  are  $38.02 \pm 0.05$   $\mu\text{mol}$  ( $73.9 \pm 0.1$

mol%) and  $11.29 \pm 0.06 \mu\text{mol}$  ( $21.9 \pm 0.1 \text{ mol}\%$ ), respectively, with  $X_{\text{CH}_4}$  of  $0.229 \pm 0.001$  (Table 2). In run COH126, by contrast, the concentrations of  $\text{H}_2\text{O}$  and  $\text{CH}_4$  increase to  $57.92 \pm 0.06 \mu\text{mol}$  ( $73.36 \pm 0.08 \text{ mol}\%$ ) and  $17.45 \pm 0.07 \mu\text{mol}$  ( $22.11 \pm 0.09 \text{ mol}\%$ ), respectively, with  $X_{\text{CH}_4}$  of  $0.232 \pm 0.001$  (Table 2). The  $\text{CH}_4/\text{Cal}_{\text{molar}}$  and  $\text{C}_{\text{tot}}/\text{Cal}_{\text{molar}}$  ratios at 2 GPa ( $0.759 \pm 0.003$  and  $0.91 \pm 0.03$ , respectively) are considerably higher than those at 1 GPa ( $0.491 \pm 0.003$  and  $0.58 \pm 0.02$ , respectively) (Fig. 2; Table 2).

### Other systems

Experiments starting with calcite without added water in the inner capsule were performed to investigate whether  $\text{CH}_4$  can be produced by dry reduction of Ca-carbonates buffered by IW in the outer capsule. The solid products and starting materials in runs COH133 and COH134 show no significant difference, other than the phase transformation of calcite into aragonite at 2 GPa and  $550 \text{ }^\circ\text{C}$  (Supplementary Data Fig. S2). Portlandite is not observed in these experiments. Run COH134 is devoid of fluids, whereas run COH133 contains very low amounts of fluid species (with a total amount of  $\sim 3 \mu\text{mol}$ ; Supplementary Data Table S2) close to the detection limit of the employed technique, likely due to the insufficient removal of adsorbed water in the inner capsule before welding.

Several CH<sub>4</sub>-generating experiments have indicated the presence of unidentified C sources that likely result from contamination (Barbier *et al.*, 2020 and references therein). To evaluate whether the silicate reactants were hosts for C-bearing materials representing the potential contaminants, we have conducted experiments starting with quartz ± water, dry synthetic chrysotile, and dry natural antigorite separately. At the studied conditions, nearly no fluids were detected in experiments starting with dry quartz (runs COH135 and COH136), whereas abundant aqueous fluids (27.96 μmol) containing negligible amounts of C-bearing species were retrieved in run COH142 starting with quartz and water (Supplementary Data Table S2). At 1 GPa and 550 °C, dehydration occurred in dry experiments starting with synthetic chrysotile (run COH195) and natural antigorite (run COH137) separately (e.g. Padrón-Navarta *et al.*, 2013; Shen *et al.*, 2015), resulting in the production of olivine (Supplementary Data Fig. S4) and abundant aqueous fluids (15.03 μmol and 68.35 μmol, respectively; Supplementary Data Table S2). In run COH195 starting with 3.60 mg of synthetic chrysotile, the fluid products contain small amounts of C-bearing species (with a total amount of ~3 μmol; Supplementary Data Table S2), probably indicative of minor C contents in the reactants. In this scenario, the lower amounts of starting chrysotile employed in runs COH201 and COH146 (0.80 mg and 0.90 mg, respectively) may have contributed at most only ~0.7 μmol of C-bearing species to the fluid products. In

run COH137, by contrast, C-bearing species are almost absent in the fluid products (Supplementary Data Table S2), reflecting nearly no C-bearing materials hosted in natural antigorite. Thus, we can conclude that C contents in the silicate reactants are insignificant and they have negligible effects on the obtained fluid compositions.

## **THERMODYNAMIC MODELLING**

Assuming equilibrium conditions, the conventional *Perple\_X* modelling was conducted to predict mainly solid phases, while the Deep Earth Water (DEW) model was used to calculate primarily aqueous fluids. Although both of them rely on thermodynamics, the DEW model in particular the EQ6 reaction path code can deal with the evolution of a water/rock system as the reaction progress, which is useful to investigate the kinetics of Ca-carbonate aqueous reduction into CH<sub>4</sub>.

### **Conventional model**

To compare phases generated in the experiments with those predicted under equilibrium conditions, as well as to investigate equilibrated phases under a wide range of  $fO_2$  and  $fH_2$  conditions, we calculated  $\log fO_2$ - $\log fH_2$  diagrams in the CaO + COH, CaO + SiO<sub>2</sub> + COH, and CaO + SiO<sub>2</sub> + MgO + COH systems both at 1 and 2 GPa at 550 °C, employing the *Perple\_X* software package (version 6.8.7; Connolly, 2005) and the internally consistent thermodynamic database of Holland

& Powell (1998) revised in 2004 (hp04ver.dat). As thermodynamic parameters of wüstite and portlandite are currently not available in this database, we added them mostly from Robie & Hemingway (1995). Solid phases were taken to be pure in the calculations while COH molecular species were described by a generic hybrid fluid EoS with non-linear subdivision (COH-Fluid+; Connolly & Galvez, 2018). The hematite–magnetite (HM), FMQ, IW, and quartz–iron–fayalite (QIF) buffers are shown for reference, corresponding to  $\log fO_2$  values of  $-16.9$ ,  $-20.5$ ,  $-26.0$ , and  $-27.8$  at 1 GPa and 550 °C, and  $-16.7$ ,  $-19.4$ ,  $-25.3$ , and  $-27.2$  at 2 GPa and 550 °C, respectively. The “fluids” routine (H–O MRK hybrid–EoS) of the Perple\_X software was used to calculate  $fH_2$  conditions in the outer capsule containing IW + H<sub>2</sub>O, showing  $\log fH_2$  values of 4.2 (1 GPa and 550 °C) and 4.9 (2 GPa and 550 °C) identical to those in the inner capsule due to H<sub>2</sub> permeability of the Au<sub>60</sub>Pd<sub>40</sub> alloy (see Section *Experimental Methods*). Compared with the well-constrained  $fO_2$  and  $fH_2$  conditions in the outer capsule (red cross in Fig. 7),  $fO_2$  values in the inner capsule are slightly lower than  $fO_2^{IW}$  where fluids mainly consist of CH<sub>4</sub> and H<sub>2</sub>O rather than pure water (see Section *Experimental Methods*).

#### *System CaO + COH*

The CH<sub>4</sub>-bearing fluids remain stable at  $\log fO_2 < -24.0$  and  $\log fH_2 > 2.7$  at 1 GPa and 550 °C, and  $\log fO_2 < -23.2$  and  $\log fH_2 > 3.6$  at 2 GPa and 550 °C (Fig. 7a and

b). In contrast, CH<sub>4</sub>-bearing fluids would be replaced by H<sub>2</sub>O-rich fluids containing minor amounts of CO<sub>2</sub> with increasing  $fO_2$  conditions, whereas Ca-carbonates and/or graphite would become the dominant C-bearing species with decreasing  $fH_2$  conditions (Fig. 7a and b). At run conditions, the equilibrated phase assemblages are portlandite and CH<sub>4</sub>-bearing fluids, indicating the  $fH_2$ -dependent Ca-carbonate reduction reaction:



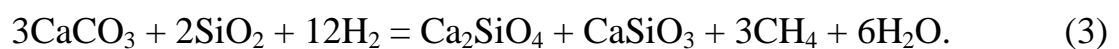
Overall, these calculations are in agreement with the experimental results, as portlandite and CH<sub>4</sub>-bearing fluids are the major products in runs COH193, COH115, COH194, and COH116 (Fig. 3 & Supplementary Data Fig. S3; Table 2). However, relicts of Ca-carbonate reactants are commonly observed in these experiments (Fig. 3; Supplementary Data Fig. S3), suggesting the incomplete reduction processes (see Section *Discussion*).

#### *System CaO + SiO<sub>2</sub> + COH*

At run conditions for these layered experiments, chemical gradients have been preserved in the inner capsule, which are favorable for investigating the kinetics of Ca-carbonate aqueous reduction into CH<sub>4</sub> (see Section *Experimental Methods*). To compare experimental run products with phases predicted under equilibrium conditions in a sliding compositional space, we calculated  $\log fO_2$ - $X_{\text{CaCO}_3}$

( $=\text{CaCO}_3/(\text{CaCO}_3 + \text{SiO}_2)_{\text{molar}}$ ) diagrams at constant  $\log f\text{H}_2$  values of 4.2 at 1 GPa and 550 °C (Supplementary Data Fig. S5a) and 4.9 at 2 GPa and 550 °C (Supplementary Data Fig. S5b), corresponding to the IW buffer. These diagrams suggest that the equilibrated phase assemblages vary with  $X_{\text{CaCO}_3}$  values under the studied  $P$ – $T$ – $f\text{O}_2$  conditions, ranging from portlandite + larnite +  $\text{CH}_4$ -bearing fluids ( $1 > X_{\text{CaCO}_3} > \sim 0.67$ ), to larnite + wollastonite +  $\text{CH}_4$ -bearing fluids ( $\sim 0.67 > X_{\text{CaCO}_3} > \sim 0.50$ ), and to wollastonite + quartz +  $\text{CH}_4$ -bearing fluids ( $\sim 0.50 > X_{\text{CaCO}_3} > 0$ ; Supplementary Data Fig. S5). Further, we calculated representative  $\log f\text{O}_2$ – $\log f\text{H}_2$  diagrams at the fixed  $\text{CaCO}_3$  and  $\text{SiO}_2$  molar ratio of 3:2 both at 1 and 2 GPa at 550 °C (Fig. 7c and d).

The  $\text{CH}_4$ -bearing fluids remain stable at  $\log f\text{O}_2 < -22.7$  and  $\log f\text{H}_2 > 2.7$  at 1 GPa and 550 °C, and  $\log f\text{O}_2 < -22.4$  and  $\log f\text{H}_2 > 3.6$  at 2 GPa and 550 °C (Fig. 7c and d). In contrast,  $\text{CH}_4$ -bearing fluids would be replaced by  $\text{H}_2\text{O}$ -rich fluids containing minor amounts of  $\text{CO}_2$  with increasing  $f\text{O}_2$  conditions, whereas Ca-carbonates and/or graphite would become the dominant C-bearing species with decreasing  $f\text{H}_2$  conditions (Fig. 7c and d). At run conditions, the equilibrated phase assemblages are larnite, wollastonite, and  $\text{CH}_4$ -bearing fluids, indicating the  $f\text{H}_2$ -dependent Ca-carbonate reduction reaction:



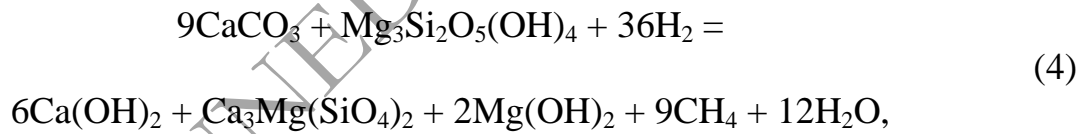
At the studied conditions, phases predicted by thermodynamic modelling (Fig. 7c and d; Supplementary Data Fig. S5) are not in accord with experimental products generated in runs COH200 and COH125 (Fig. 4; Table 2). Moreover, starting Ca-carbonates and quartz commonly appear as relicts in these experiments (Fig. 4), suggesting the incomplete reduction processes (see Section *Discussion*).

#### *System CaO + SiO<sub>2</sub> + MgO + COH*

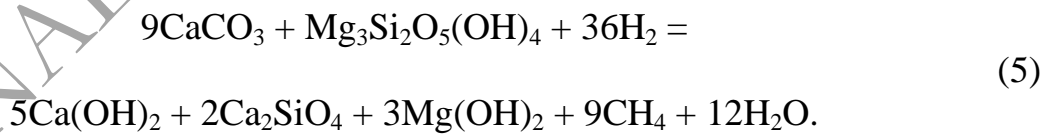
Similar to calculations performed in the CaO + SiO<sub>2</sub> + COH system, log  $fO_2$ – $X'_{CaCO_3}$  ( $=CaCO_3/(CaCO_3 + Mg_3Si_2O_5(OH)_4)_{molar}$ ) diagrams were calculated at constant log  $fH_2$  values of 4.2 at 1 GPa and 550 °C (Supplementary Data Fig. S6a) and 4.9 at 2 GPa and 550 °C (Supplementary Data Fig. S6b), corresponding to the IW buffer. These diagrams suggest that  $X'_{CaCO_3}$  values play an important role in regulating the equilibrated phase assemblages under the studied  $P$ – $T$ – $fO_2$  conditions. At 1 GPa for  $X'_{CaCO_3} > \sim 0.67$ , the equilibrated phase assemblages are portlandite + merwinite + brucite + CH<sub>4</sub>-bearing fluids ( $1 > X'_{CaCO_3} > \sim 0.75$ ) and monticellite + merwinite + brucite + CH<sub>4</sub>-bearing fluids ( $\sim 0.75 > X'_{CaCO_3} > \sim 0.67$ ; Supplementary Data Fig. S6a). At 2 GPa for  $X'_{CaCO_3} > \sim 0.75$ , the equilibrated phase assemblages are portlandite + larnite + brucite + CH<sub>4</sub>-bearing fluids ( $1 > X'_{CaCO_3} > \sim 0.80$ ) and larnite + merwinite + brucite + CH<sub>4</sub>-bearing fluids ( $\sim 0.80 > X'_{CaCO_3} > \sim 0.75$ ; Supplementary Data Fig. S6b). Further, we calculated representative log

$fO_2$ – $\log fH_2$  diagrams at the fixed  $CaCO_3$  and  $Mg_3Si_2O_5(OH)_4$  molar ratio of 9:1 both at 1 and 2 GPa at 550 °C (Fig. 7e and f).

The  $CH_4$ -bearing fluids remain stable at  $\log fO_2 < -22.8$  and  $\log fH_2 > 2.7$  at 1 GPa and 550 °C, and  $\log fO_2 < -22.6$  and  $\log fH_2 > 3.6$  at 2 GPa and 550 °C (Fig. 7e and f). In contrast,  $CH_4$ -bearing fluids would be replaced by  $H_2O$ -rich fluids containing minor amounts of  $CO_2$  with increasing  $fO_2$  conditions, whereas Ca-carbonates and/or graphite would become the dominant C-bearing species with decreasing  $fH_2$  conditions (Fig. 7e and f). At run conditions, the equilibrated phase assemblages are portlandite + merwinite + brucite +  $CH_4$ -bearing fluids (1 GPa) and portlandite + larnite + brucite +  $CH_4$ -bearing fluids (2 GPa), indicating the  $fH_2$ -dependent Ca-carbonate reduction reactions:



and



At the studied conditions of 1 GPa, thermodynamically predicted phases (Fig. 7e; Supplementary Data Fig. S6a) are not in agreement with experimentally generated products in runs COH201 and COH146 (Fig. 5a–c; Table 2). By contrast, the assemblage of portlandite + larnite + brucite +  $CH_4$ -bearing fluids produced in

run COH147 (Fig. 5d–f; Table 2) has been predicted by thermodynamic modelling at 2 GPa (Fig. 7f; Supplementary Data Fig. S6b). In particular, relicts of Ca-carbonate reactants have been rarely or never observed in runs COH146 and COH147 characterized by long run durations (Fig. 5), suggesting that the reduction processes are almost complete (see Section *Discussion*).

### **DEW model in the CaO + COH system**

To investigate the reaction progress of Ca-carbonate aqueous reduction under the studied conditions, we performed thermodynamic calculations in the representative CaO + COH system using the DEW model (Sverjensky *et al.*, 2014; Huang & Sverjensky, 2019) and the EQ3/EQ6 software (Wolery, 1992; Wolery & Daveler, 1992) with a modified Berman database (Berman, 1988). The speciation–solubility code EQ3 was used to calculate reduced fluid compositions at  $P = 1$  GPa,  $T = 550$  °C, and  $\log fO_2 = -26.0$  corresponding to the IW buffer, where C molalities were set to make the fluids saturated with portlandite. At the same  $P$ – $T$  conditions, the reaction path modelling code EQ6 was further used to model the interactions between the EQ3 fluids containing 1.0 kg of H<sub>2</sub>O and a given number of calcite calculated based on the fluid/rock (F/R) ratios. Test calculations were conducted at different F/R ratios of 0.5 and 2, while their results are nearly identical.

The evolution of minerals, dissolved elements and species in the fluids, and  $fO_2$  and  $fH_2$  conditions as a function of the reaction progress (in logarithm) at 1 GPa and 550 °C for the F/R ratio of 2 is shown in Fig. 8. The reaction proceeds with the progressive growth of portlandite by replacing calcite, where calcite reactant is completely consumed as the reaction nears completion (Fig. 8a). The dissolved C and Ca contents in the fluids remain almost unchanged at the onset of the reaction, while they start to increase at log reaction progress of about  $-2.5$  and  $0$ , respectively (Fig. 8b). The model predicts high relative concentrations of  $CH_4$  in the fluids, and its evolution during the reaction is similar to that of the dissolved C (Fig. 8b and c). When the reaction is close to completion, concentrations of aqueous C-bearing species significantly increase in the fluids, including  $CH_4$ ,  $HCOO^-$ ,  $CH_3COO^-$ ,  $CO$ ,  $CO_2$ ,  $H_2CO_3$ ,  $HCO_3^-$ , and  $CO_3^{2-}$  (Fig. 8c). The initial  $fO_2$  of the IW buffer, as well as  $fH_2$ , remains nearly unchanged until at reaction completion when the former increases to  $\log fO_2 \approx -23.0$  ( $\Delta FMQ \approx -3$ ) while the latter decreases to  $\log fH_2 \approx 2.7$  (Fig. 8d). As a result, the evolution at log reaction progress higher than  $\sim 0$  is characterized by an increase in  $fO_2$  but a decrease in  $fH_2$ , contributing to portlandite growth at the expense of calcite, and the elevated molalities of dissolved C and Ca elements as well as aqueous C-bearing species in the fluids (Fig. 8). In this study, however, the double capsule technique has fixed  $fH_2$  (and thus  $fO_2$ ) conditions throughout the experiments (see Section *Experimental*

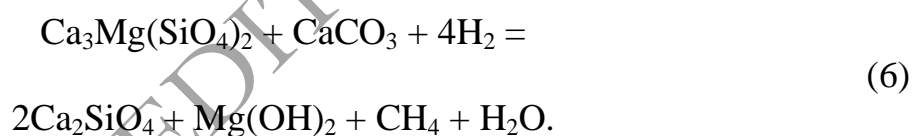
*Methods*), indicating that the reduction processes proceed at log reaction progress lower than  $\sim 0$  (Fig. 8).

## DISCUSSION

### Comparison between experimental and thermodynamic modelling results

In this study, Ca-carbonate reactants commonly occur as relicts in the run products, particularly in experiments starting with calcite + water, calcite + quartz + water, and calcite + natural antigorite + water (Figs. 3, 4 and 6). However, phase assemblages predicted by thermodynamic modelling at run conditions indicate that Ca-carbonates would be metastable if equilibrium were reached in these experiments (Fig. 7 and 8a). Since the IW buffer constrained  $fH_2$  values in both inner and outer capsules throughout the runs (see Section *Experimental Methods*), the incomplete consumption of Ca-carbonates in the presence of reduced fluids (Table 2) is likely attributed to short run durations. Although the intermediate products in the layered experiments have potentially hindered further reactions between Ca-carbonates and silicates especially in the  $CaO + SiO_2 + COH$  system, the fluids can flow throughout the inner capsule as reflected by the relatively loosely packed mineral grains filled with pores (Fig. 4). In this scenario,  $CH_4$  production may proceed firstly in the  $CaO + SiO_2 + COH$  system and subsequently in the  $CaO + COH$  system, which does not considerably affect our discussion

below with respect to the kinetics-controlled Ca-carbonate aqueous reduction into CH<sub>4</sub>. At 1 GPa and 550 °C, thermodynamic calculations in the CaO + SiO<sub>2</sub> + MgO + COH system demonstrate that the equilibrated phase assemblage is comprised of portlandite, merwinite, brucite, and CH<sub>4</sub>-bearing fluids (Fig. 7e). In contrast, products in runs COH201 and COH146 are mainly composed of portlandite, larnite, brucite, and CH<sub>4</sub>-bearing fluids, as well as calcite relicts, whereas merwinite appears as inclusions in larnite commonly intergrown with brucite (Fig. 5a–c). These thermodynamic constraints and microstructures suggest that merwinite in these experiments may have been largely consumed by calcite to form larnite and brucite:



Based on the negligible calcite relicts in run COH146, as well as its CH<sub>4</sub>/Cal<sub>molar</sub> ratio of ~1, the newly formed phase assemblage of portlandite + larnite + brucite + CH<sub>4</sub>-bearing fluids may have been close to re-equilibrium, as reflected by the long run duration of 240 h for the experiment. At 2 GPa and 550 °C, the phase assemblage of portlandite + larnite + brucite + CH<sub>4</sub>-bearing fluids generated in run COH147 is consistent with that predicted by thermodynamic modelling in the CaO + SiO<sub>2</sub> + MgO + COH system (Fig. 7f), suggesting that equilibrium was almost attained in the experiment. This is in agreement with the long run duration of 264 h

for run COH147 causing the complete consumption of Ca-carbonate reactant (Fig. 5d–f).

### **Kinetics-controlled Ca-carbonate aqueous reduction into CH<sub>4</sub>**

Overall, comparisons of experimental run products with thermodynamically predicted phase assemblages indicate that equilibrium has not yet been attained in most of the studied runs (see above). Time-series experiments conducted in representative systems at 1 GPa and 550 °C provide evidence for the duration-controlled Ca-carbonate aqueous reduction into CH<sub>4</sub>, with the CH<sub>4</sub>/Ca<sub>molar</sub> ratios ranging from ~0.13 at 24 h (run COH193), to ~0.33 at 72 h (run COH115), and to ~0.41 at 240 h (run COH194) in the CaO + COH system, and from ~0.85 at 72 h (run COH201) to ~1.00 at 240 h (run COH146) in the CaO + SiO<sub>2</sub> + MgO + COH (synthetic Cl-bearing chrysotile) system (Fig. 2; Table 2). Based on these ratios, we have retrieved rate constants of  $0.8 \times 10^{-6} \text{ s}^{-1}$  and  $7.4 \times 10^{-6} \text{ s}^{-1}$  for such kinetics-controlled reactions in the CaO + COH and CaO + SiO<sub>2</sub> + MgO + COH (synthetic Cl-bearing chrysotile) systems, respectively (Fig. 9). For comparison, the rate constants of  $4.0 \times 10^{-6} \text{ s}^{-1}$  and  $2.6 \times 10^{-6} \text{ s}^{-1}$  were also calculated for reactions in the CaO + SiO<sub>2</sub> + COH and CaO + SiO<sub>2</sub> + MgO + COH (natural Fe–Al-bearing antigorite) systems, respectively, despite their limited experimental data (Fig. 9). These constraints demonstrate that equilibrium can be nearly attained at run

durations of ~2400 h, ~500 h, ~250 h, and ~750 h in experiments starting with calcite + water, calcite + quartz + water, calcite + synthetic chrysotile + water, and calcite + natural antigorite + water, respectively (Fig. 9).

At 1 GPa and 550 °C, the  $\text{CH}_4/\text{Cal}_{\text{molar}}$  ratios in experiments starting with calcite + quartz + water (run COH200), calcite + synthetic chrysotile + water (run COH201), and calcite + natural antigorite + water (run COH119) are higher than the ratio in run COH115 starting with calcite + water at the same run duration of 72 h (Fig. 2), indicating that addition of silicates can potentially enhance the efficiency of calcite reduction into  $\text{CH}_4$ . At these conditions, the calculated rate constants for the silicate-involving reactions are about 3–9 times higher than the constant for the silicate-absent reaction (Fig. 9). In contrast to run COH200, the relatively lower  $\text{CH}_4/\text{Cal}_{\text{molar}}$  ratio in run COH119 is probably because starting antigorite contains small amounts of  $\text{Fe}^{3+}$  (Vitale Brovarone *et al.*, 2017), thereby leading to  $f\text{O}_2$  slightly higher than the IW buffer responsible for the reduction processes. Conversely, the relatively higher  $\text{CH}_4/\text{Cal}_{\text{molar}}$  ratio in run COH201 is probably attributed to the incorporation of ~1 wt% Cl in starting chrysotile during its synthesis (Villa *et al.*, 2018), which may increase the aqueous solubility of calcite (Newton & Manning, 2002) and thus promote  $\text{CH}_4$  generation through Reaction (7):



and/or Reaction (8):



The acceleration of Ca-carbonate aqueous reduction in the presence of silicates has also been recorded at 2 GPa and 550 °C by comparing the  $\text{CH}_4/\text{Ca}_{\text{molar}}$  ratios in runs COH116 and COH125 with the same run duration of 72 h, whereas the longer duration of 96 h for run COH126 may compensate for the negative effects of  $\text{Fe}^{3+}$  in starting antigorite (Vitale Brovarone *et al.*, 2017) and thus contribute to its higher  $\text{CH}_4/\text{Ca}_{\text{molar}}$  ratio (Fig. 2). The positive role of silicates in these reduction processes is inferred to be mainly associated with the dissolved  $\text{SiO}_2$  in aqueous fluids (Tumiati *et al.*, 2017, 2020), which has promoted Ca-carbonate dissolution through synthesizing Ca–Si-bearing complexes (e.g.  $\text{Ca}(\text{HSiO}_3)^+$ ; Huang & Sverjensky, 2019) and thus accelerated  $\text{CH}_4$  production. In contrast, Ca–Mg-bearing complexes are relatively hard to be synthesized in the fluids, indicating that the MgO component in serpentines may have not significantly affected the reduction efficiency of Ca-carbonates. Besides the addition of silicates, an increase in pressures is also favorable for Ca-carbonate reduction into  $\text{CH}_4$  at comparable run conditions (cf. runs COH115 and COH116, runs COH200 and COH125, and runs COH119 and COH126), despite their variable accelerating trends (Fig. 2). This is probably related to Ca-carbonate aqueous solubility increasing with pressures under subduction zone conditions (e.g. Newton & Manning, 2002; Caciagli & Manning, 2003). However, since experiments in this study were only

performed at a fixed temperature of 550 °C, the potential effects of variable temperatures on HP aqueous reduction of Ca-carbonates would be beyond the scope of discussion.

### **Stability of CH<sub>4</sub> and/or graphite through HP aqueous reduction of C-bearing materials**

The experimental and thermodynamic modelling results suggest that products contain copious amounts of CH<sub>4</sub>-bearing fluids while graphite is never observed at run conditions (see above). The current study, together with other reduction experiments starting with carbonate minerals or organic matter (e.g. carboxylic acids and carboxylates) and water at variable oxygen buffers (Sharma *et al.*, 2009; Lazar *et al.*, 2014; Li, 2017; Mukhina *et al.*, 2017), demonstrates the strong dependence of CH<sub>4</sub> and graphite stabilities on  $fO_2$  under subduction zone conditions (Fig. 10). It is apparent that CH<sub>4</sub> (with or without other short-chain hydrocarbons), relative to graphite, is the dominant C-bearing species at low  $fO_2$  buffered by Fe, IW/IM, or WM under a wide range of  $P$ – $T$  conditions (Fig. 10). At increasing  $fO_2$  buffered by Co–CoO or Ni–NiO, by contrast, decomposition of carbonate minerals or organic matter would result in the concomitant formation of CH<sub>4</sub> and graphite (Fig. 10). This is in agreement with field-based studies showing the coexistence of CH<sub>4</sub> and graphite through Fe-bearing dolomite aqueous

reduction at  $\Delta\text{FMQ}$   $-2.5$  to  $-1.5$  at  $2.5$ – $3.0$  GPa and  $500$ – $575$  °C (between the WM and Co–CoO buffers) in carbonated eclogites from the Chinese southwestern Tianshan (Tao *et al.*, 2018) and calcite methanation induced by  $\text{H}_2$ -riched fluids at  $\Delta\text{FMQ}$   $-6.0$  to  $-3.0$  at  $1.0$ – $2.0$  GPa and  $400$ – $500$  °C (between the WM and Co–CoO buffers) in opicalcites from the Italian Western Alps (Vitale Brovarone *et al.*, 2017; Giuntoli *et al.*, 2020). At more oxidized conditions buffered by Re– $\text{ReO}_2$ , decomposition of carbonate minerals or organic matter would be characterized by the precipitation of graphite but the absence of  $\text{CH}_4$  (Fig. 10). Thus, these experiments suggest that *HP* aqueous reduction of carbonate minerals or organic matter buffered by WM or below may generate  $\text{CH}_4$  (possibly with other short-chain hydrocarbons) as the dominant C-bearing species, which would be gradually replaced by graphite with the increasing  $f\text{O}_2$ . Nevertheless, due to the lack of experiments on *HP* aqueous reduction of C-bearing materials at  $f\text{O}_2$  above the WM buffer at relatively lower temperatures (e.g.  $< 600$  °C), it is undetermined whether  $\text{CH}_4$  and/or graphite can remain stable under these conditions.

The absence of graphite through *HP* aqueous reduction of carbonate minerals or organic matter at low  $f\text{O}_2$  (Fig. 10) is probably due to the coupled  $f\text{O}_2$  and  $f\text{H}_2$  in a closed hydrous system, in which low  $f\text{O}_2$  represents high  $f\text{H}_2$  that may promote the hydrogenation of graphite forming  $\text{CH}_4$  (e.g. Sharma *et al.*, 2009; Vitale Brovarone *et al.*, 2017; Peña-Alvarez *et al.*, 2021). To further investigate the

dependence of graphite stability on  $fO_2$  in a nearly anhydrous system, we calculated  $\log fO_2$ - $P$  diagrams at very low  $fH_2$  (e.g.  $\log fH_2 = -2.0$ ) and a fixed temperature of 550 °C in the CaO + C, CaO + SiO<sub>2</sub> + C, and CaO + SiO<sub>2</sub> + MgO + C systems. In the CaO + C system, the onset of graphite precipitation through Ca-carbonate anhydrous reduction happens at  $fO_2$  below the IW buffer but close to the QIF buffer under the studied  $P$ - $T$  conditions (Supplementary Data Fig. S7a). In contrast, calculations in the CaO + SiO<sub>2</sub> + C and CaO + SiO<sub>2</sub> + MgO + C systems at representative starting compositions suggest that anhydrous graphitization of Ca-carbonates starts at  $\Delta FMQ$  -2 to -1 under the studied  $P$ - $T$  conditions (Supplementary Data Fig. S7b and c). However, these calculations are relatively hard to be confirmed experimentally, where extremely long run durations would be required due to the lack of fluid medium (e.g. Holloway & Wood, 1988).

### **Geological implications**

Our data provide experimental evidence for kinetics-controlled abiotic CH<sub>4</sub> production through Ca-carbonate reduction in the CaO + COH, CaO + SiO<sub>2</sub> + COH, and CaO + SiO<sub>2</sub> + MgO + COH systems under subduction zone  $P$ - $T$  conditions, induced by aqueous fluids at low  $fO_2$  close to the IW buffer. In natural subduction zone settings, however, the redox nature of slab-derived fluids remains largely controversial. Taking subducted serpentinites as an example, rock-based studies,

theoretical calculations, and experimental simulations suggest that dehydration of these rocks at eclogite facies may generate highly oxidized fluids (Debret *et al.*, 2014, 2015; Debret & Sverjensky, 2017; Maurice *et al.*, 2020). In contrast, petrological investigation and thermodynamic modelling demonstrate that reduced fluids containing H<sub>2</sub> or H<sub>2</sub>S can be released during prograde deserpentinization (Peretti *et al.*, 1992; Piccoli *et al.*, 2019). Redox states of the fluids liberated from subducted serpentinites are inferred to depend on a combination of factors, including the hydration extent of their protoliths before entering subduction zones (Evans *et al.*, 2017; Evans & Frost, 2021). Subducted serpentinites experiencing intense pre-subduction seawater alteration discharge oxidized fluids in equilibrium with mainly magnetite, whereas those recording less pervasive seawater–rock interactions release reduced fluids that are equilibrated with both awaruite (FeNi<sub>3</sub>) and magnetite corresponding to the IM buffer (Carbonin *et al.*, 2015). Therefore, dehydration of subducted serpentinites can potentially liberate highly reduced fluids. Other than deserpentinization, HP serpentinization of ultramafic rocks at depths of or greater than 20–30 km in subduction zones, as suggested by natural observations and thermodynamic calculations, may also represent a possible source of reduced fluids that commonly contain some amounts of H<sub>2</sub> (Li *et al.*, 2007, 2010; Vitale Brovarone *et al.*, 2017, 2020; Lazar, 2020). An infiltration of such reduced fluids derived from deserpentinization or serpentinization at forearc depths would

be conducive to aqueous reduction of subducted Ca-carbonates into CH<sub>4</sub>, thereby providing potential insights into C mobility in subduction zones.

At 1 GPa and 550 °C, the reaction rate constant retrieved in the CaO + COH system indicates that equilibrium can be nearly attained at the run duration of ~2400 h, while the addition of silicates would reduce the durations required for equilibrium to less than ~750 h (Fig. 9). Thus, silicate involvement can enhance the reduction efficiency at relatively short durations of several months before the complete consumption of Ca-carbonate reactants. At longer durations, the kinetics-controlled reduction processes of Ca-carbonates would reach equilibrium, leading to their molar ratios between CH<sub>4</sub> and starting calcite representing the reaction progress consistent with those containing silicate reactants (Fig. 9). Nevertheless, Ca-carbonate reactants are commonly preserved in natural HP reduced rocks (e.g. CH<sub>4</sub>-bearing ophicalcites from the Italian Western Alps; Vitale Brovarone *et al.*, 2017; Giuntoli *et al.*, 2020), indicative of the incomplete Ca-carbonate reduction into CH<sub>4</sub> at convergent margins. The overall slab dehydration processes are considered to be continuous over millions of years under a wide range of *P–T* conditions, whereas the individual fluid flow events in subduction zones may be much faster and highly channelized (John *et al.*, 2012). These slab-derived fluids are mobilized in a short-lived and pulse-like character, as indicated by lithium chronometry, corresponding to timescales of the fluid–rock interactions as short as

hundreds of years to several months (Penniston-Dorland *et al.*, 2010; John *et al.*, 2012; Taetz *et al.*, 2018). Furthermore, natural reaction rates, especially in regional metamorphic environments, are regarded as slower than those predicted by laboratory experiments (Baxter, 2003; Baxter & Depaolo, 2004). In this scenario, the experimentally constrained durations required for equilibrium (Fig. 9) may underestimate the amounts of time for the completion of fluid–rock interactions in natural subduction zone settings (e.g. Penniston-Dorland *et al.*, 2010). Besides the addition of silicates, an increase in pressures can also enhance the reduction efficiency of Ca-carbonates as reactions proceed (Fig. 2). As a result, our experimental data provide potential implications for short-lived fluid–rock interactions in subduction zones, where the production of CH<sub>4</sub> through kinetics-controlled Ca-carbonate aqueous reduction may be accelerated by involving silicates and/or increasing pressures. However, uncertainties remain regarding the widespread application of the experimentally constrained kinetic models to natural settings, considering the variability in fluid compositions and fluid to rock ratios at convergent margins (e.g. Sieber *et al.*, 2020).

## CONCLUSIONS

By using calcite + water ± quartz ± serpentine (synthetic Cl-bearing chrysotile and natural Fe–Al-bearing antigorite) as starting materials, we have performed

experiments on kinetics-controlled Ca-carbonate aqueous reduction into CH<sub>4</sub> in the CaO + COH, CaO + SiO<sub>2</sub> + COH, and CaO + SiO<sub>2</sub> + MgO + COH systems buffered by IW both at 1 and 2 GPa at 550 °C. Experimental run products contain portlandite ± larnite ± wollastonite ± brucite as well as Ca-carbonate and/or silicate reactants, and copious amounts of CH<sub>4</sub>-bearing aqueous fluids characterized by variable molar ratios between CH<sub>4</sub> and starting calcite ( $\text{CH}_4/\text{Ca}_{\text{mol}} = \sim 0.13$  to  $\sim 1.00$ ) reflecting different degrees of reaction completion. Thermodynamic calculations demonstrate that equilibrium has not yet been attained in most of the studied runs, while reaction kinetics play an important role in controlling these reduction processes as evidenced by time-series experiments. The retrieved rate constants for reactions in the SiO<sub>2</sub>-bearing systems are about 3–9 times higher than the constant in the CaO + COH system ( $0.8 \times 10^{-6} \text{ s}^{-1}$ ), suggesting that the addition of silicates can considerably shorten the durations required for equilibrium of Ca-carbonate aqueous reduction. As reactions proceed, an increase in pressures is also favorable for the production of CH<sub>4</sub>. Our work indicates that Ca-carbonate reduction at forearc depths, triggered by aqueous fluids at  $f\text{O}_2$  of IW, represents a possible source of abiotic CH<sub>4</sub> in subduction zones and thus provides potential insights into the mobility of subducted C. The reduction efficiency can be enhanced by involving silicates and/or increasing pressures in particular through the short-lived fluid–rock interactions.

## **DATA AVAILABILITY**

The data underlying this article are available in the article and in its online supplementary material.

## **SUPPLEMENTARY DATA**

Supplementary data are available at *Journal of Petrology* online.

## **FUNDING**

This work was supported by the National Key Research and Development Program of China (No. 2019YFA0708501), by an Italian program MIUR PRIN (No. 2017ZE49E7\_002) and MIUR Levi Montalcini, and by a Richard Lounsbery Foundation grant. This work is part of a project that has received funding from the European Research Council (ERC) under the European Union's Horizon 2020 research and innovation programme (Grant agreement No. 864045). Carla Tiraboschi acknowledges support from the German Research Foundation (DFG Grant TI 1078/2-1).

## **ACKNOWLEDGEMENTS**

We thank Marcello Campione and Chiara Groppo for providing synthetic chrysotile and natural antigorite, respectively. We are grateful to Andrea

Risplendente for his assistance during microprobe analysis and to Andrea Amalfa for preparing some of the experiments. The authors wish to acknowledge Matthieu Galvez, Melanie Sieber, and Codi Lazar for their detailed and constructive comments that have substantially improved the manuscript. Jörg Hermann is greatly appreciated for his editorial handling and helpful suggestions.

## References

- Arai, S., Ishimaru, S. & Mizukami, T. (2012). Methane and propane micro-inclusions in olivine in titanoclinohumite-bearing dunites from the Sanbagawa high-P metamorphic belt, Japan: Hydrocarbon activity in a subduction zone and Ti mobility. *Earth and Planetary Science Letters* **353**, 1–11.
- Barbier, S., Huang, F., Andreani, M., Tao, R., Hao, J., Eleish, A., Prabhu, A., Minhas, O., Fontaine, K., Fox, P. & Daniel, I. (2020). A review of H<sub>2</sub>, CH<sub>4</sub>, and hydrocarbon formation in experimental serpentinization using network analysis. *Frontiers in Earth Science* **8**, 209.
- Baxter, E. F. (2003). *Natural constraints on metamorphic reaction rates*. In: Vance, D., Müller, W. & Villa, I. M. (eds.) *Geochronology: Linking the Isotopic Record with Petrology and Textures*. Geological Society, London, Special Publications **220**, 183–202.
- Baxter, E. F. & DePaolo, D. J. (2004). Can metamorphic reactions proceed faster than bulk strain? *Contributions to Mineralogy and Petrology* **146**, 657–670.
- Berman, R. G. (1988). Internally-consistent thermodynamic data for minerals in the system Na<sub>2</sub>O–K<sub>2</sub>O–CaO–MgO–FeO–Fe<sub>2</sub>O<sub>3</sub>–Al<sub>2</sub>O<sub>3</sub>–SiO<sub>2</sub>–TiO<sub>2</sub>–H<sub>2</sub>O–CO<sub>2</sub>. *Journal of Petrology* **29**, 445–522.

- Bose, K. & Ganguly, J. (1995). Quartz-coesite transition revisited: Reversed experimental determination at 500–1200 °C and retrieved thermochemical properties. *American Mineralogist* **80**, 231–238.
- Boutier, A., Vitale Brovarone, A., Martinez, I., Sissmann, O. & Mana, S. (2021). High-pressure serpentinization and abiotic methane formation in metaperidotite from the Appalachian subduction, northern Vermont. *Lithos* **396–397**, 106190.
- Caciagli, N. C. & Manning, C. E. (2003). The solubility of calcite in water at 6–16 kbar and 500–800 °C. *Contributions to Mineralogy and Petrology* **146**, 275–285.
- Carbonin, S., Martin, S., Tumiati, S. & Rossetti, P. (2015). Magnetite from the Cogne serpentinites (Piemonte ophiolite nappe, Italy). Insights into seafloor fluid–rock interaction. *European Journal of Mineralogy* **27**, 31–50.
- Connolly, J. A. D. (2005). Computation of phase equilibria by linear programming: A tool for geodynamic modeling and its application to subduction zone decarbonation. *Earth and Planetary Science Letters* **236**, 524–541.
- Connolly, J. A. D. & Galvez, M. E. (2018). Electrolytic fluid speciation by Gibbs energy minimization and implications for subduction zone mass transfer. *Earth and Planetary Science Letters* **501**, 90–102.
- Consuma, G., Braga, R., Giovanardi, T., Bersani, D., Konzett, J., Lugli, F., Mazzucchelli, M. & Tropper, P. (2020). *In situ* Sr isotope analysis of mantle carbonates: Constraints on the evolution and sources of metasomatic carbon-bearing fluids in a paleo-collisional setting. *Lithos* **354–355**, 105334.
- Debret, B. & Sverjensky, D. A. (2017). Highly oxidising fluids generated during serpentinite breakdown in subduction zones. *Scientific Reports* **7**, 10351.
- Debret, B., Andreani, M., Muñoz, M., Bolfan-Casanova, N., Carlut, J., Nicollet, C., Schwartz, S. & Trcera, N. (2014). Evolution of Fe redox state in serpentine during subduction. *Earth and Planetary Science Letters* **400**, 206–218.

- Debret, B., Bolfan-Casanova, N., Padrón-Navarta, J. A., Martin-Hernandez, F., Andreani, M., Garrido, C. J., López Sánchez-Vizcaíno, V., Gómez-Pugnaire, M. T., Muñoz, M. & Trcera, N. (2015). Redox state of iron during high-pressure serpentinite dehydration. *Contributions to Mineralogy and Petrology* **169**, 36.
- Etioppe, G. & Schoell, M. (2014). Abiotic gas: Atypical, but not rare. *Elements* **10**, 291–296.
- Etioppe, G. & Sherwood Lollar, B. (2013). Abiotic Methane on Earth. *Reviews of Geophysics* **51**, 276–299.
- Eugster, H. P. & Skippen, G. B. (1967). Igneous and metamorphic reactions involving gas equilibria. *Researches in Geochemistry* **2**, 492–520.
- Eugster, H. P. & Wones, D. R. (1962). Stability relations of the Ferruginous biotite, annite. *Journal of Petrology* **3**, 82–125.
- Evans, K. A. (2012). The redox budget of subduction zones. *Earth-Science Reviews* **113**, 11–32.
- Evans, K. A. & Frost, B. R. (2021). Deserpentinization in subduction zones as a source of oxidation in arcs: A reality check. *Journal of Petrology* **62**, egab016.
- Evans, K. A., Reddy, S. M., Tomkins, A. G., Crossley, R. J. & Frost, B. R. (2017). Effects of geodynamic setting on the redox state of fluids released by subducted mantle lithosphere. *Lithos* **278–281**, 26–42.
- Galvez, M. E. & Pubellier, M. (2019). *How do subduction zones regulate the carbon cycle?* In: Orcutt, B. N., Daniel, I. & Dasgupta, R. (eds.) *Deep carbon: Past to Present*. Cambridge University Press, 276–312.
- Giuntoli, F., Vitale Brovarone, A. & Menegon, L. (2020). Feedback between high-pressure genesis of abiotic methane and strain localization in subducted carbonate rocks. *Scientific Reports* **10**, 9848.
- Groat, L. A., Hawthorne, F. C. & Ercit, T. S. (1992). The chemistry of vesuvianite. *Canadian Mineralogist* **30**, 19–48.

- Hayes, J. M. & Waldbauer, J. R. (2006). The carbon cycle and associated redox processes through time. *Philosophical Transactions of The Royal Society B* **361**, 931–950.
- Holland, T. J. B. & Powell, R. (1998). An internally consistent thermodynamic data set for phases of petrological interest. *Journal of Metamorphic Geology* **16**, 309–343.
- Holloway, J. R. & Wood, B. J. (1988). *Simulating the Earth: Experimental Geochemistry*. London: Unwin Hyman.
- Hu, H., Vitale Brovarone, A., Zhang, L., Piccoli, F., Peng, W. & Shen, T. (2021). Retrograde carbon sequestration in orogenic complexes: A case study from the Chinese southwestern Tianshan. *Lithos* **392–393**, 106151.
- Huang, F. & Sverjensky, D. A. (2019). Extended Deep Earth Water model for predicting major element mantle metasomatism. *Geochimica et Cosmochimica Acta* **254**, 192–230.
- Huang, F., Daniel, I., Cardon, H., Montagnac, G. & Sverjensky, D. A. (2017). Immiscible hydrocarbon fluids in the deep carbon cycle. *Nature Communications* **8**, 15798.
- Jaeckel, K., Bebout, G. E. & Angiboust, S. (2018). Deformation-enhanced fluid and mass transfer along Western and Central Alps paleo-subduction interfaces: Significance for carbon cycling models. *Geosphere* **14**, 2355–2375.
- Jenkins, D. M. & Bozhilov, K. N. (2003). Stability and thermodynamic properties of ferro-actinolite: A re-investigation. *American Journal of Science* **303**, 723–752.
- John, T., Gussone, N., Podladchikov, Y. Y., Bebout, G. E., Dohmen, R., Halama, R., Klemd, R., Magna, T. & Seitz, H.-M. (2012). Volcanic arcs fed by rapid pulsed fluid flow through subducting slabs. *Nature Geoscience* **5**, 489–492.

- Kelley, D. S., Karson, J. A., Früh-Green, G. L., Yoerger, D. R., Shank, T. M., Butterfield, D. A., Hayes, J. M., Schrenk, M. O., Olson, E. J., Proskurowski, G., Jakuba, M., Bradley, A., Larson, B., Ludwig, K., Glickson, D., Buckman, K., Bradley, A. S., Brazelton, W. J., Roe, K., Elend, M. J., Delacour, A., Bernasconi, S. M., Lilley, M. D., Baross, J. A., Summons, R. E. & Sylva, S. P. (2005). A serpentinite-hosted ecosystem: The Lost City hydrothermal field. *Science* **307**, 1428–1434.
- Klein, F., Grozeva, N. G. & Seewald, J. S. (2019). Abiotic methane synthesis and serpentinization in olivine-hosted fluid inclusions. *Proceedings of the National Academy of Sciences of the United States of America* **116**, 17666–17672.
- Lazar, C. (2020). Using silica activity to model redox-dependent fluid compositions in serpentinites from 100 to 700 °C and from 1 to 20 kbar. *Journal of Petrology* **61**, egaa101.
- Lazar, C., Zhang, C., Manning, C. E. & Mysen, B. O. (2014). Redox effects on calcite-portlandite-fluid equilibria at forearc conditions: Carbon mobility, methanogenesis, and reduction melting of calcite. *American Mineralogist* **99**, 1604–1615.
- Li, Y. (2017). Immiscible C-H-O fluids formed at subduction zone conditions. *Geochemical Perspectives Letters* **3**, 12–21.
- Li, X.-P., Zhang, L., Wei, C., Ai, Y. & Chen, J. (2007). Petrology of rodingite derived from eclogite in western Tianshan, China. *Journal of Metamorphic Geology* **25**, 363–382.
- Li, X.-P., Zhang, L.-F., Wilde, S. A., Song, B. & Liu, X.-M. (2010). Zircons from rodingite in the Western Tianshan serpentinite complex: mineral chemistry and U–Pb ages define nature and timing of rodingitization. *Lithos* **118**, 17–34.
- Luth, R. W. (1989). Natural versus experimental control of oxidation state: Effects on the composition and speciation of C-O-H fluids. *Geofluids* **74**, 50–57.

- Matveev, S., Ballhaus, C., Fricke, K., Truckenbrodt, J. & Ziegenbein, D. (1997). Volatiles in the Earth's mantle: I. Synthesis of CHO fluids at 1273 K and 2.4 GPa. *Geochimica et Cosmochimica Acta* **61**, 3081–3088.
- Maurice, J., Bolfan-Casanova, N., Demouchy, S., Chauvigne, P., Schiavi, F. & Debret, B. (2020). The intrinsic nature of antigorite breakdown at 3 GPa: Experimental constraints on redox conditions of serpentinite dehydration in subduction zones. *Contributions to Mineralogy and Petrology* **175**, 94.
- McCollom, T. M. & Seewald, J. S. (2013). Serpentinites, hydrogen, and life. *Elements* **9**, 129–134.
- Ménez, B. (2020). Abiotic hydrogen and methane: Fuels for life. *Elements* **16**, 39–46.
- Miozzi, F. & Tumiatì, S. (2020). Aqueous concentration of CO<sub>2</sub> in carbon-saturated fluids as a highly sensitive oxybarometer. *Geochemical Perspectives Letters* **16**, 30–34.
- Mukhina, E., Kolesnikov, A. & Kutcherov, V. (2017). The lower pT limit of deep hydrocarbon synthesis by CaCO<sub>3</sub> aqueous reduction. *Scientific Reports* **7**, 5749.
- Newton, R. C. & Manning, C. E. (2002). Experimental determination of calcite solubility in H<sub>2</sub>O–NaCl solutions at deep crust/upper mantle pressures and temperatures: Implications for metasomatic processes in shear zones. *American Mineralogist* **87**, 1401–1409.
- Okamoto, A., Oyanagi, R., Yoshida, K., Uno, M., Shimizu, H. & Satish-Kumar, M. (2021). Rupture of wet mantle wedge by self-promoting carbonation. *Communications Earth & Environment* **2**, 151.
- Padrón-Navarta, J. A., López Sánchez-Vizcaíno, V., Hermann, J., Connolly, J. A. D., Garrido, C. J., Gómez-Pugnaire, M. T. & Marchesi, C. (2013). Tschermak's substitution in antigorite and consequences for phase relations and water liberation in high-grade serpentinites. *Lithos* **178**, 186–196.

- Peña-Alvarez, M., Vitale Brovarone, A., Donnelly, M.-E., Wang, M., Dalladay-Simpson, P., Howie, R. & Gregoryanz, E. (2021). In-situ abiogenic methane synthesis from diamond and graphite under geologically relevant conditions. *Nature Communications* **12**, 6387.
- Peng, W., Zhang, L., Menzel, M. D., Vitale Brovarone, A., Tumiati, S., Shen, T. & Hu, H. (2020). Multistage CO<sub>2</sub> sequestration in the subduction zone: Insights from exhumed carbonated serpentinites, SW Tianshan UHP belt, China. *Geochimica et Cosmochimica Acta* **270**, 218–243.
- Peng, W., Zhang, L., Tumiati, S., Vitale Brovarone, A., Hu, H. & Shen, T. (2021). Abiotic methane generation through reduction of serpentinite-hosted dolomite: Implications for carbon mobility in subduction zones. *Geochimica et Cosmochimica Acta* **311**, 119–140.
- Penniston-Dorland, S. C., Sorensen, S. S., Ash, R. D. & Khadke, S. V. (2010). Lithium isotopes as a tracer of fluids in a subduction zone mélange: Franciscan Complex, CA. *Earth and Planetary Science Letters* **292**, 181–190.
- Peretti, A., Dubessy, J., Mullis, J., Frost, B. R. & Trommsdorff, V. (1992). Highly reducing conditions during Alpine metamorphism of the Malenco peridotite (Sondrio, northern Italy) indicated by mineral paragenesis and H<sub>2</sub> in fluid inclusions. *Contributions to Mineralogy and Petrology* **112**, 329–340.
- Piccoli, F., Vitale Brovarone, A., Beyssac, O., Martinez, I., Ague, J. J. & Chaduteau, C. (2016). Carbonation by fluid–rock interactions at high-pressure conditions: Implications for carbon cycling in subduction zones. *Earth and Planetary Science Letters* **445**, 146–159.
- Piccoli, F., Vitale Brovarone, A. & Ague, J. J. (2018). Field and petrological study of metasomatism and high-pressure carbonation from lawsonite eclogite-facies terrains, Alpine Corsica. *Lithos* **304–307**, 16–37.

- Piccoli, F., Hermann, J., Pettke, T., Connolly, J. A. D., Kempf, E. D. & Vieira Duarte, J. F. (2019). Subducting serpentinites release reduced, not oxidized, aqueous fluids. *Scientific Reports* **9**, 19573.
- Piccoli, F., Ague, J. J., Chu, X., Tian, M. & Vitale Brovarone, A. (2021). Field-based evidence for intra-slab high-permeability channel formation at eclogite-facies conditions during subduction. *Geochemistry, Geophysics, Geosystems* **22**, e2020GC009520.
- Plümper, O., King, H. E., Geisler, T., Liu, Y., Pabst, S., Savoy, I. P., Rost, D. & Zack, T. (2017). Subduction zone forearc serpentinites as incubators for deep microbial life. *Proceedings of the National Academy of Sciences of the United States of America* **114**, 4324–4329.
- Robie, R. A. & Hemingway, B. S. (1995). *Thermodynamic Properties of Minerals and Related Substances at 298.15 K and 1 Bar (10<sup>5</sup> Pascals) Pressure and at Higher Temperatures*. U.S. Geological Survey Bulletin **2131**.
- Russell, M. J., Hall, A. J. & Martin, W. (2010). Serpentinization as a source of energy at the origin of life. *Geobiology* **8**, 355–371.
- Sachan, H. K., Mukherjee, B. K. & Bodnar, R. J. (2007). Preservation of methane generated during serpentinization of upper mantle rocks: Evidence from fluid inclusions in the Nidar ophiolite, Indus Suture Zone, Ladakh (India). *Earth and Planetary Science Letters* **257**, 47–59.
- Scambelluri, M., Bebout, G. E., Belmonte, D., Gilio, M., Campomenosi, N., Collins, N. & Crispini, L. (2016). Carbonation of subduction-zone serpentinite (high-pressure ophicarbonates; Ligurian Western Alps) and implications for the deep carbon cycling. *Earth and Planetary Science Letters* **441**, 155–166.
- Scott, H. P., Hemley, R. J., Mao, H., Herschbach, D. R., Fried, L. E., Howard, W. M. & Bastea, S. (2004). Generation of methane in the Earth's mantle: *In situ* high pressure–temperature measurements of carbonate reduction. *Proceedings*

*of the National Academy of Sciences of the United States of America* **101**, 14023–14026.

Sharma, A., Cody, G. D. & Hemley, R. J. (2009). *In situ* diamond-anvil cell observations of methanogenesis at high pressures and temperatures. *Energy & Fuels* **23**, 5571–5579.

Sheik, C. S., Cleaves II, H. J., Johnson-Finn, K., Giovannelli, D., Kieft, T. L., Papineau, D., Schrenk, M. O. & Tumati, S. (2020). Abiotic and biotic processes that drive carboxylation and decarboxylation reactions. *American Mineralogist* **105**, 609–615.

Shen, T., Hermann, J., Zhang, L., Lü, Z., Padrón-Navarra, J. A., Xia, B. & Bader, T. (2015). UHP metamorphism documented in Ti-chondrodite- and Ti-clinohumite-bearing serpentinized ultramafic rocks from Chinese southwestern Tianshan. *Journal of Petrology* **56**, 1425–1458.

Shi, G. U., Tropper, P., Cui, W., Tan, J. & Wang, C. (2005). Methane (CH<sub>4</sub>)-bearing fluid inclusions in the Myanmar jadeitite. *Geochemical Journal* **39**, 503–516.

Sieber, M. J., Hermann, J. & Yaxley, G. M. (2018). An experimental investigation of C–O–H fluid-driven carbonation of serpentinites under forearc conditions. *Earth and Planetary Science Letters* **496**, 178–188.

Sieber, M. J., Yaxley, G. M. & Hermann, J. (2020). Investigation of fluid-driven carbonation of a hydrated, forearc mantle wedge using serpentinite cores in high-pressure experiments. *Journal of Petrology* **61**, egaa035.

Sieber, M. J., Yaxley, G. M. & Hermann, J. (2022). COH-fluid induced metasomatism of peridotites in the forearc mantle. *Contributions to Mineralogy and Petrology* **177**, 44.

- Song, S., Su, L., Niu, Y., Lai, Y. & Zhang, L. (2009). CH<sub>4</sub> inclusions in orogenic harzburgite: Evidence for reduced slab fluids and implications for redox melting in mantle wedge. *Geochimica et Cosmochimica Acta* **73**, 1737–1754.
- Spránitz, T., Padrón-Navarta, J. A., Szabó, C., Szabó, A. & Berkesi, M. (2022). Abiotic passive nitrogen and methane enrichment during exhumation of subducted rocks: Primary multiphase fluid inclusions in high-pressure rocks from the Cabo Ortegal Complex, NW Spain. *Journal of Metamorphic Geology*, 1–29. <https://doi.org/10.1111/jmg.12666>.
- Sverjensky, D. A., Harrison, B. & Azzolini, D. (2014). Water in the deep Earth: The dielectric constant and the solubilities of quartz and corundum to 60 kb and 1200 °C. *Geochimica et Cosmochimica Acta* **129**, 125–145.
- Syracuse, E. M., van Keken, P. E. & Abers, G. A. (2010). The global range of subduction zone thermal models. *Physics of the Earth and Planetary Interiors* **183**, 73–90.
- Taetz, S., John, T., Bröcker, M., Spandler, C. & Stracke A. (2018). Fast intraslab fluid-flow events linked to pulses of high pore fluid pressure at the subducted plate interface. *Earth and Planetary Science Letters* **482**, 33–43.
- Tao, R., Zhang, L., Tian, M., Zhu, J., Liu, X., Liu, J., Höfer, H. E., Stagno, V. & Fei, Y. (2018). Formation of abiotic hydrocarbon from reduction of carbonate in subduction zones: Constraints from petrological observation and experimental simulation. *Geochimica et Cosmochimica Acta* **239**, 390–408.
- Tiraboschi, C., Tumiati, S., Recchia, S., Miozzi, F. & Poli, S. (2016). Quantitative analysis of COH fluids synthesized at HP–HT conditions: an optimized methodology to measure volatiles in experimental capsules. *Geofluids* **16**, 841–855.
- Tiraboschi, C., Tumiati, S., Sverjensky, D., Pettke, T., Ulmer, P. & Poli, S. (2018). Experimental determination of magnesia and silica solubilities in graphite-

saturated and redox-buffered high-pressure COH fluids in equilibrium with forsterite + enstatite and magnesite + enstatite. *Contributions to Mineralogy and Petrology* **173**, 2.

Tiraboschi, C., Miozzi, F. & Tumiati, S. (2022). Carbon-saturated COH fluids in the upper mantle: a review of high-pressure and high-temperature ex situ experiments. *European Journal of Mineralogy* **34**, 59–75.

Truche, L., McCollom, T. M. & Martinez, I. (2020). Hydrogen and abiotic hydrocarbons: Molecules that change the world. *Elements* **16**, 13–18.

Tumiati, S. & Malaspina, N. (2019). Redox processes and the role of carbon-bearing volatiles from the slab–mantle interface to the mantle wedge. *Journal of the Geological Society* **176**, 388–397.

Tumiati, S., Fumagalli, P., Tiraboschi, C. & Poli, S. (2013). An experimental study on COH-bearing peridotite up to 3.2 GPa and implications for crust–mantle recycling. *Journal of Petrology* **54**, 453–479.

Tumiati, S., Godard, G., Martin, S., Malaspina, N. & Poli, S. (2015). Ultra-oxidized rocks in subduction mélanges? Decoupling between oxygen fugacity and oxygen availability in a Mn-rich metasomatic environment. *Lithos* **226**, 116–130.

Tumiati, S., Tiraboschi, C., Sverjensky, D. A., Pettke, T., Recchia, S., Ulmer, P., Miozzi, F. & Poli, S. (2017). Silicate dissolution boosts the CO<sub>2</sub> concentrations in subduction fluids. *Nature Communications* **8**, 616.

Tumiati, S., Tiraboschi, C., Miozzi, F., Vitale-Brovarone, A., Manning, C. E., Sverjensky, D. A., Milani, S. & Poli, S. (2020). Dissolution susceptibility of glass-like carbon versus crystalline graphite in high-pressure aqueous fluids and implications for the behavior of organic matter in subduction zones. *Geochimica et Cosmochimica Acta* **273**, 383–402.

- Villa, C., Campione, M., Santiago-González, B., Alessandrini, F., Erratico, S., Zucca, I., Bruzzone, M. G., Forzenigo, L., Malatesta, P., Mauri, M., Trombetta, E., Brovelli, S., Torrente, Y., Meinardi, F. & Monguzzi, A. (2018). Self-assembled pH-sensitive fluoromagnetic nanotubes as archetype system for multimodal imaging of brain cancer. *Advanced Functional Materials* **28**, 1707582.
- Vitale Brovarone, A., Martinez, I., Elmaleh, A., Compagnoni, R., Chaduteau, C., Ferraris, C. & Esteve, I. (2017). Massive production of abiotic methane during subduction evidenced in metamorphosed ophiocarbonates from the Italian Alps. *Nature Communications* **8**, 14134.
- Vitale Brovarone, A., Sverjensky, D. A., Piccoli, F., Ressico, F., Giovannelli, D. & Daniel, I. (2020). Subduction hides high-pressure sources of energy that may feed the deep subsurface biosphere. *Nature Communications* **11**, 3880.
- Whitney, D. L. & Evans, B. W. (2010). Abbreviations for names of rock-forming minerals. *American Mineralogist* **95**, 185–187.
- Wolery, T. J. (1992). *EQ3NR, A Computer Program for Geochemical Aqueous Speciation-Solubility Calculations: Theoretical Manual, User's Guide, and Related Documentation (Version 7.0); Part 3*. Lawrence Livermore National Laboratory.
- Wolery, T. J. & Daveler, S. A. (1992). *EQ6, A Computer Program for Reaction Path Modeling of Aqueous Geochemical Systems: Theoretical Manual, User's Guide, and Related Documentation (Version 7.0); Part 4*. Lawrence Livermore National Laboratory.
- Zhang, L., Wang, Q., Ding, X. & Li, W.-C. (2021). Diverse serpentinization and associated abiotic methanogenesis within multiple types of olivine-hosted fluid inclusions in orogenic peridotite from northern Tibet. *Geochimica et Cosmochimica Acta* **296**, 1–17.

**Table 1:** Chemical formulas and abbreviations of phases in this study

| Phase           | Formula <sup>I</sup>   | Abbreviation <sup>II</sup> |
|-----------------|--|----------------------------|
| Antigorite      | $Mg_{x(48-4y)}Fe_{(1-x)(48-4y)}Al_{8y}Si_{34-4y}O_{85}(OH)_{62}$ | Atg                        |
| Aragonite       | $CaCO_3$   | Arg                        |
| Brucite         | $Mg(OH)_2$   | Brc                        |
| Calcite         | $CaCO_3$   | Cal                        |
| Carbon dioxide  | $CO_2$   | –                          |
| Carbon monoxide | $CO$   | –                          |
| Chlorite        | $Mg_{x(6-y)}Fe_{(1-x)(6-y)}Al_{2y}Si_{4-y}O_{10}(OH)_8$          | Chl                        |
| Chrysotile      | $Mg_3Si_2O_5(OH)_4$  | Ctl                        |
| Diopside        | $CaMgSi_2O_6$  | Di                         |
| Dolomite        | $CaMg(CO_3)_2$   | Dol                        |
| Fayalite        | $Fe_2SiO_4$  | Fa                         |
| Forsterite      | $Mg_2SiO_4$  | Fo                         |
| Graphite        | $C$  | Gr                         |
| Hematite        | $Fe_2O_3$  | Hem                        |
| Hydrogen        | $H_2$  | –                          |
| Iron            | $Fe$   | –                          |
| Larnite         | $Ca_2SiO_4$  | Lrn                        |
| Lime            | $CaO$  | –                          |
| Magnetite       | $Fe_3O_4$  | Mag                        |
| Methane         | $CH_4$   | –                          |
| Merwinite       | $Ca_3Mg(SiO_4)_2$  | Mw                         |
| Monticellite    | $CaMgSiO_4$  | Mtc                        |
| Olivine         | $(Mg,Fe)_2SiO_4$   | Ol                         |
| Oxygen          | $O_2$  | –                          |
| Periclase       | $MgO$  | Per                        |
| Portlandite     | $Ca(OH)_2$   | Port                       |
| Quartz          | $SiO_2$  | Q                          |
| Spurrite        | $Ca_5(SiO_4)_2CO_3$  | Spu                        |
| Vesuvianite     | $Ca_{19}(Mg,Fe,Al)_{13}Si_{18}O_{68}(OH,F,O)_{10}$               | Ves                        |
| Water           | $H_2O$   | –                          |
| Wollastonite    | $CaSiO_3$  | Wo                         |
| Wüstite         | $FeO$  | Wus                        |

<sup>I</sup> Formulas of antigorite and chlorite are from Padrón-Navarta *et al.* (2013) while vesuvianite from Groat *et al.* (1992).

<sup>II</sup> Abbreviations are mostly from Whitney & Evans (2010).

**Table 2:** Run table of experiments

| Run  | P<br>(GPa) | T<br>(°C) | Starting material             | Composition of starting material<br>(mg/μmol) |               |               |               |                  | X <sub>Ca</sub> <sup>I</sup> | Time<br>(h) | Solid product                        |
|--|------------|-----------|-------------------------------|---|---------------|---------------|---------------|------------------|------------------------------|-------------|--------------------------------------|
|  |            |           |                               | Cal   | Q             | Ctl           | Atg           | H <sub>2</sub> O |                              |             |                                      |
| <i>System CaO + COH</i>  |            |           |                               |   |               |               |               |                  |                              |             |                                      |
| COH 193  | 1          | 550       | Cal, H <sub>2</sub> O         | 4.20/<br>42.0                                 | –             | –             | –             | 1.20/<br>66.6    | 1.0<br>0                     | 24          | Port, Cal                            |
| COH 115  | 1          | 550       | Cal, H <sub>2</sub> O         | 4.20/<br>42.0                                 | –             | –             | –             | 1.00/<br>55.5    | 1.0<br>0                     | 72          | Port, Cal                            |
| COH 194  | 1          | 550       | Cal, H <sub>2</sub> O         | 4.20/<br>42.0                                 | –             | –             | –             | 1.30/<br>72.2    | 1.0<br>0                     | 240         | Port, Cal                            |
| COH 116  | 2          | 550       | Cal, H <sub>2</sub> O         | 3.80/<br>38.0                                 | –             | –             | –             | 1.00/<br>55.5    | 1.0<br>0                     | 72          | Port, Arg                            |
| <i>System CaO + SiO<sub>2</sub> + COH</i>  |            |           |                               |   |               |               |               |                  |                              |             |                                      |
| COH 200  | 1          | 550       | Cal, Q,<br>H <sub>2</sub> O   | 2.60/<br>26.0                                 | 2.60/<br>43.3 | –             | –             | 0.80/<br>44.4    | 0.3<br>8                     | 72          | Port, Lrn, Wo, Cal,<br>Q             |
| COH 125  | 2          | 550       | Cal, Q,<br>H <sub>2</sub> O   | 2.60/<br>26.0                                 | 2.00/<br>33.3 | –             | –             | 0.90/<br>50.0    | 0.4<br>4                     | 72          | Port, Lrn, Wo, Arg,<br>Q             |
| COH 121  | 2          | 550       | Cal, Q,<br>H <sub>2</sub> O   | 2.10/<br>21.0                                 | 2.80/<br>46.6 | –             | –             | 0.90/<br>50.0    | 0.3<br>1                     | 72          | Port, Lrn, Wo, Arg,<br>Q             |
| <i>System CaO + SiO<sub>2</sub> + MgO + COH (synthetic Cl-bearing chrysotile)</i>  |            |           |                               |   |               |               |               |                  |                              |             |                                      |
| COH 201  | 1          | 550       | Cal, Ctl,<br>H <sub>2</sub> O | 2.40/<br>24.0                                 | –             | 0.80/<br>2.90 | –             | 0.90/<br>50.0    | 0.8<br>9                     | 72          | Port, Lrn, Brc, Mw,<br>Cal           |
| COH 146  | 1          | 550       | Cal, Ctl,<br>H <sub>2</sub> O | 2.40/<br>24.0                                 | –             | 0.90/<br>3.26 | –             | 1.00/<br>55.5    | 0.8<br>8                     | 240         | Port, Lrn, Brc, Mw,<br>Cal           |
| COH 147  | 2          | 550       | Cal, Ctl,<br>H <sub>2</sub> O | 2.80/<br>28.0                                 | –             | 1.40/<br>5.07 | –             | 1.10/<br>61.1    | 0.8<br>5                     | 264         | Port, Lrn, Brc                       |
| <i>System CaO + SiO<sub>2</sub> + MgO + COH (natural Fe–Al-bearing antigorite)</i> |            |           |                               |   |               |               |               |                  |                              |             |                                      |
| COH 119  | 1          | 550       | Cal, Atg,<br>H <sub>2</sub> O | 2.30/<br>23.0                                 | –             | –             | 0.79/<br>0.17 | 1.00/<br>55.5    | 0.9<br>9                     | 72          | Port, Lrn, Brc, Mtc,<br>Ol, Chl, Cal |
| COH 126  | 2          | 550       | Cal, Atg,<br>H <sub>2</sub> O | 2.30/<br>23.0                                 | –             | –             | 1.30/<br>0.29 | 0.90/<br>50.0    | 0.9<br>9                     | 96          | Port, Lrn, Brc, Mw,<br>Ves, Arg      |

**Table 2:** Run table of experiments (continue)

| Run  | Total fluid  | Concentration of fluid species ( $\mu\text{mol}$ ) |               |               |             | Concentration of fluid species (mol%) |               |               |             | $X_{\text{CH}_4}^{\text{II}}$ | $\text{CH}_4/\text{Cal}^{\text{III}}$<br>molar | $C_{\text{tot}}/\text{Cal}^{\text{IV}}$<br>molar |
|--|--|--|---------------|---------------|-------------|---------------------------------------|---------------|---------------|-------------|-------------------------------|--|--|
|  |  | $\text{H}_2\text{O}$                               | $\text{CH}_4$ | $\text{CO}_2$ | $\text{CO}$ | $\text{H}_2\text{O}$                  | $\text{CH}_4$ | $\text{CO}_2$ | $\text{CO}$ |                               |  |  |
| <i>System CaO + COH</i>  |  |  |               |               |             |                                       |               |               |             |                               |  |  |
| COH 193  | 11.62  | 4.3(2)   | 5.5(1)        | 0.00(9)       | 1(2)        | 39(2)                                 | 51(1)         | 0.0(8)        | 10(15)      | 0.56(2)                       | 0.131(3)                                       | 0.16(4)  |
| COH 115  | 49.25  | 33.77(9)   | 13.9(1)       | 0.31(8)       | 1.3(7)      | 68.6(2)                               | 28.2(2)       | 0.6(2)        | 3(1)        | 0.292(2)                      | 0.331(2)                                       | 0.37(2)  |
| COH 194  | 27.29  | 3.4(2)   | 17.4(1)       | 0.0(1)        | 7(2)        | 12.3(7)                               | 63.6(5)       | 0.0(4)        | 24(7)       | 0.838(9)                      | 0.413(3)                                       | 0.57(5)  |
| COH 116  | 83.81  | 56.2(2)  | 23.7(2)       | 0.5(2)        | 2(2)        | 68.1(2)                               | 28.7(3)       | 0.7(2)        | 3(2)        | 0.297(2)                      | 0.624(5)                                       | 0.69(5)  |
| <i>System CaO + SiO<sub>2</sub> + COH</i>  |  |  |               |               |             |                                       |               |               |             |                               |  |  |
| COH 200  | 44.20  | 23.15(4)   | 16.78(3)      | 0.09(2)       | 1.3(4)      | 56.0(1)                               | 40.60(7)      | 0.22(5)       | 3.1(9)      | 0.420(1)                      | 0.645(1)                                       | 0.70(2)  |
| COH 125  | 55.60  | 31.79(6)   | 17.24(7)      | 0.14(6)       | 3.0(5)      | 60.9(1)                               | 33.0(1)       | 0.3(1)        | 6(1)        | 0.352(1)                      | 0.663(3)                                       | 0.78(3)  |
| COH 121  | Capsule broken but selected for petrographic observation |  |               |               |             |                                       |               |               |             |                               |  |  |
| <i>System CaO + SiO<sub>2</sub> + MgO + COH (synthetic Cl-bearing chrysotile)</i>  |  |  |               |               |             |                                       |               |               |             |                               |  |  |
| COH 201  | 58.10  | 33.8(1)  | 20.46(9)      | 0.22(6)       | 0(1)        | 62.0(2)                               | 37.6(2)       | 0.4(1)        | 0(2)        | 0.377(2)                      | 0.853(4)                                       | 0.89(3)  |
| COH 146  | 39.83  | 14.4(3)  | 24.0(2)       | 0.1(2)        | 0(3)        | 37.4(7)                               | 62.2(6)       | 0.4(4)        | 0(7)        | 0.625(7)                      | 1.000(9)                                       | 1.06(7)  |
| COH 147  | 6.72   | 1.34(3)  | 2.70(2)       | 0.03(2)       | 0.0(3)      | 32.9(7)                               | 66.4(6)       | 0.7(5)        | 0(8)        | 0.668(7)                      | —  |  |
| <i>System CaO + SiO<sub>2</sub> + MgO + COH (natural Fe-Al-bearing antigorite)</i> |  |  |               |               |             |                                       |               |               |             |                               |  |  |
| COH 119  | 59.36  | 38.02(5)   | 11.29(6)      | 0.20(5)       | 1.9(5)      | 73.9(1)                               | 21.9(1)       | 0.40(9)       | 3.8(9)      | 0.229(1)                      | 0.491(3)                                       | 0.58(2)  |
| COH 126  | 85.77  | 57.92(6)   | 17.45(7)      | 0.16(5)       | 3.4(5)      | 73.36(8)                              | 22.11(9)      | 0.20(7)       | 4.3(6)      | 0.232(1)                      | 0.759(3)                                       | 0.91(3)  |

<sup>I</sup> $X_{\text{Cal}} = \text{Cal}/(\text{Cal} \pm \text{Q} \pm \text{CtI} \pm \text{Atg})_{\text{molar}}$ ; <sup>II</sup> $X_{\text{CH}_4} = \text{CH}_4/(\text{CH}_4 + \text{H}_2\text{O})_{\text{molar}}$ ; <sup>III</sup>Molar ratio between the generated

$\text{CH}_4$  and starting calcite; <sup>IV</sup>Molar ratio between the generated total C-bearing species (including  $\text{CH}_4$ ,  $\text{CO}_2$ , and  $\text{CO}$ ) and starting calcite.

## FIGURE CAPTIONS

**Fig. 1.** (a–c) Schematic illustration of the double capsule system. The inner  $\text{Au}_{60}\text{Pd}_{40}$  capsule contains starting materials, including (a) calcite + water, (b) layered calcite + quartz + water, and (c) layered calcite + serpentine (synthetic Cl-bearing chrysotile and natural Fe–Al-bearing antigorite) + water. The outer Au capsule contains the inner capsule and the IW +  $\text{H}_2\text{O}$  buffering assemblage. Due to  $\text{H}_2$  permeability of the  $\text{Au}_{60}\text{Pd}_{40}$  alloy,  $f\text{H}_2$  conditions are homogeneous in the inner and outer capsules. (d) Back-scattered electron image showing the preservation of iron and wüstite in the outer capsule after quenching. (e) The  $\log f\text{O}_2$ – $P$  diagram calculated at a fixed temperature of 550 °C for a variety of oxygen buffers. Mineral abbreviations in this study follow Whitney & Evans (2010).

**Fig. 2.** Molar ratios between the generated  $\text{CH}_4$  and starting calcite ( $\text{CH}_4/\text{Cal}_{\text{molar}}$ ) in the experiments, with run numbers denoted. The larger symbol sizes represent the longer run durations (24 h, 72 h, 96 h, and 240 h). Hollow and solid symbols represent experiments at 1 GPa and 2 GPa, respectively.

**Fig. 3.** Solid products in runs (a–c) COH193 and (d–f) COH194 ( $P = 1$  GPa,  $T = 550$  °C). Portlandite crystals grow at the expense of calcite grains, with the portlandite selvage width in run COH194 larger than that in run COH193.

**Fig. 4.** Solid products in run COH121 ( $P = 2$  GPa,  $T = 550$  °C). (a) Back-scattered electron image and (b) compositional X-ray map showing the layered distribution of portlandite, larnite, and wollastonite between aragonite and quartz.

**Fig. 5.** Solid products in runs (a–c) COH146 ( $P = 1$  GPa,  $T = 550$  °C) and (d–f) COH147 ( $P = 2$  GPa,  $T = 550$  °C). (a & b) Growth of portlandite and larnite (in

association with brucite) by replacing calcite, with merwinite inclusions visible in larnite. (c) Relatively even distribution of portlandite, larnite, and brucite. (d–f) Mineral assemblage of portlandite, larnite, and brucite, with the latter two commonly showing an intergrown texture.

**Fig. 6.** Solid products in runs (a–c) COH119 ( $P = 1$  GPa,  $T = 550$  °C) and (d & e) COH126 ( $P = 2$  GPa,  $T = 550$  °C). (a) Cross section of the capsule showing solid products in the inner Au<sub>60</sub>Pd<sub>40</sub> capsule and the IW buffer in the outer Au capsule. Starting calcite is partly replaced by the newly formed phases including portlandite. (b & c) Enlargement of boxes in (a) showing the occurrence of larnite, brucite, and monticellite (enclosing small amounts of forsterite-rich olivine) as well as chlorite. (d) Portlandite having aragonite inclusions and coexisting with larnite. (e) Intergrowths of larnite and brucite, with merwinite and vesuvianite visible.

**Fig. 7.** Phase stabilities under variable  $fO_2$  and  $fH_2$  conditions in the (a & b) CaO + COH, (c & d) CaO + SiO<sub>2</sub> + COH (with the CaCO<sub>3</sub> and SiO<sub>2</sub> molar ratio of 3:2), and (e & f) CaO + SiO<sub>2</sub> + MgO + COH (with the CaCO<sub>3</sub> and Mg<sub>3</sub>Si<sub>2</sub>O<sub>5</sub>(OH)<sub>4</sub> molar ratio of 9:1) systems both at 1 and 2 GPa at 550 °C. Orange dashed lines show log  $fO_2$  values of the HM, FMQ, IW, and QIF buffers. The red cross constrains  $fO_2$  and  $fH_2$  values in the outer capsule while  $fO_2$  conditions in the inner capsule are slightly lower than  $fO_2^{IW}$  (see text for details).

**Fig. 8.** Evolution of (a) minerals (including calcite reactant and portlandite product, as well as calcite consumed in the reaction), (b & c) dissolved elements and species in the fluids, and (d)  $fO_2$  and  $fH_2$  conditions through interactions between reduced fluids and calcite in the CaO + COH system at 1 GPa and 550 °C for the F/R ratio

of 2. Each unit of the reaction progress variable corresponds to destruction of 1.0 mol of calcite reactant and mixing with the EQ3 fluids containing 1.0 kg of H<sub>2</sub>O.

**Fig. 9.** Reaction rate constants retrieved on the basis of molar ratios between the generated CH<sub>4</sub> and starting calcite (CH<sub>4</sub>/Cal<sub>molar</sub>) and run durations at 1 GPa and 550 °C. Due to the limited experimental data, rate constants for reactions starting with calcite + quartz + water and calcite + natural antigorite + water were roughly constrained.

**Fig. 10.** Results of representative experiments on HP aqueous reduction of carbonate minerals or organic matter at variable  $f_{O_2}$  under subduction zone conditions (data from Sharma *et al.*, 2009; Lazar *et al.*, 2014; Li, 2017; Mukhina *et al.*, 2017; and this study). For comparison,  $P$ – $T$ – $f_{O_2}$  conditions for abiogenic CH<sub>4</sub> generation through HP carbonate reduction in natural samples from the Italian Western Alps (Vitale Brovarone *et al.*, 2017; Giuntoli *et al.*, 2020) and the Chinese southwestern Tianshan (Tao *et al.*, 2018) are shown. Grey and black colors filled in symbols represent the presence of CH<sub>4</sub> and graphite, respectively. The purple and light purple areas display the modelled prograde  $P$ – $T$  paths of subduction zones at the slab interface and slab Moho, respectively (Syracuse *et al.*, 2010).

Fig. 1.

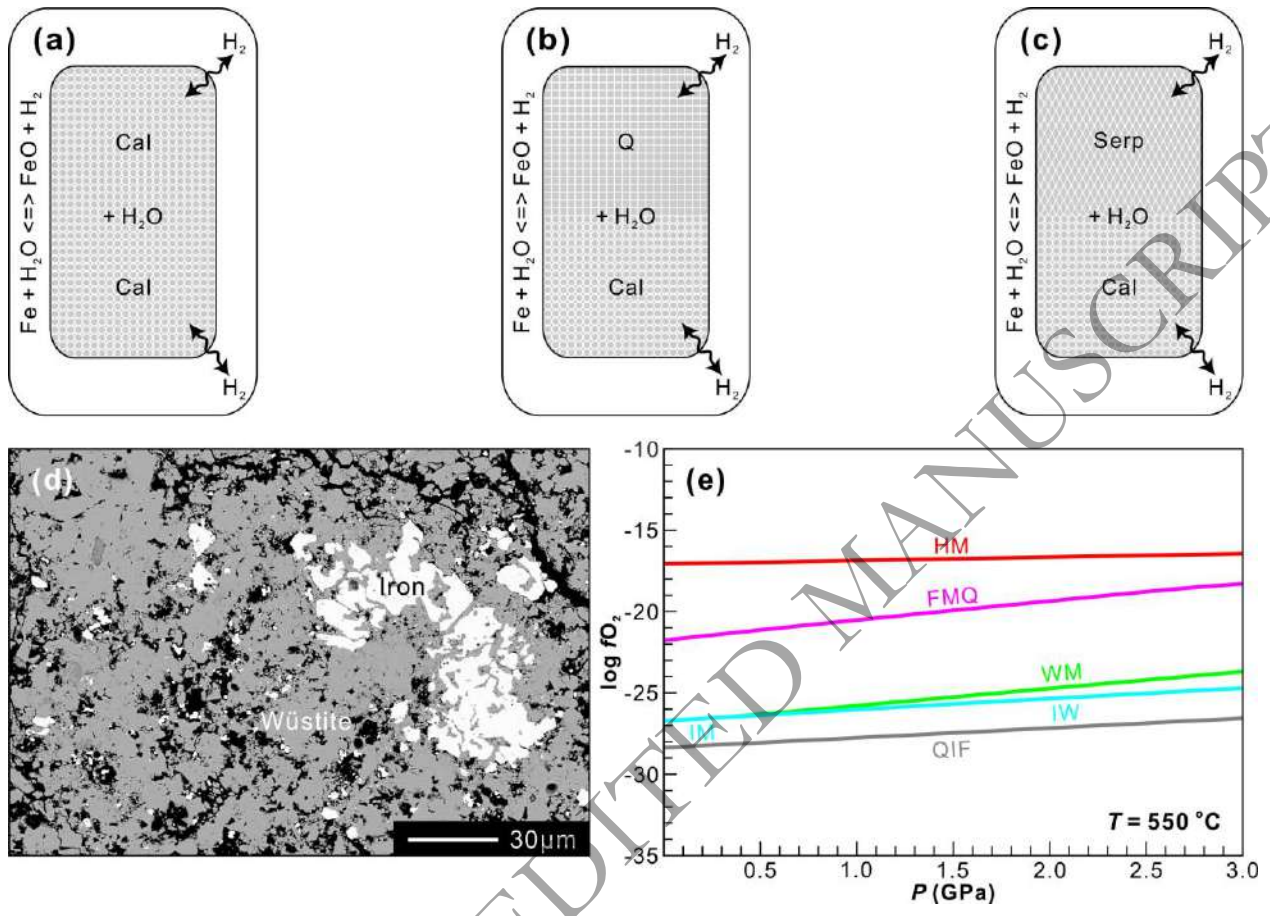
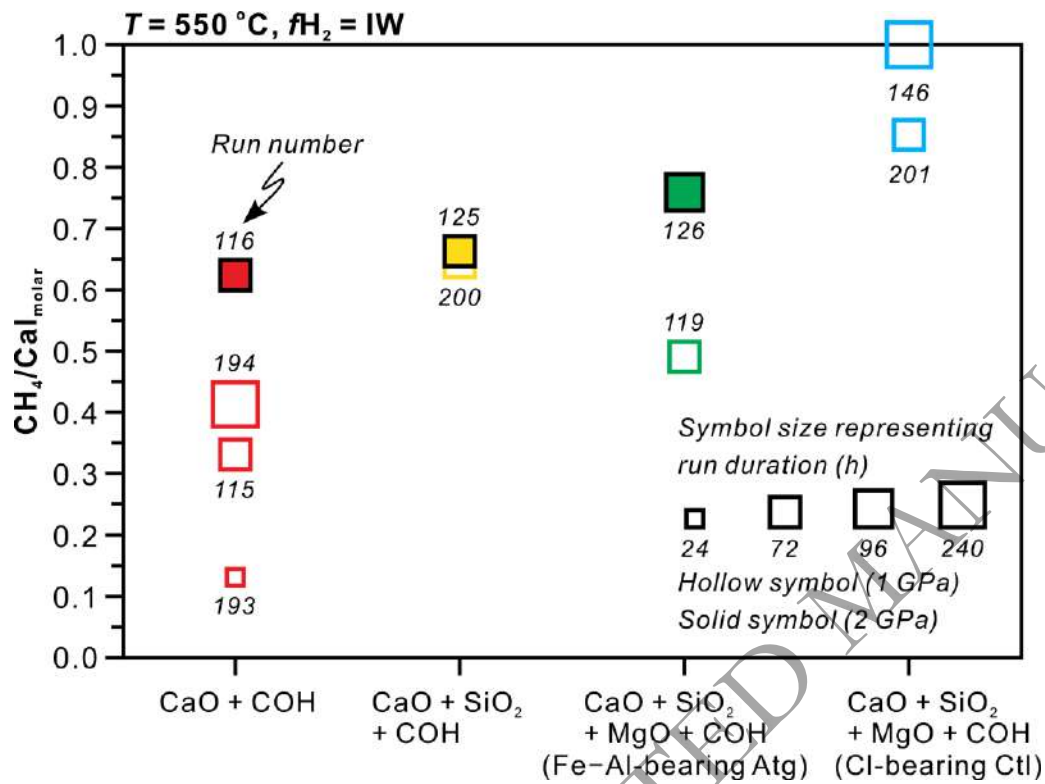
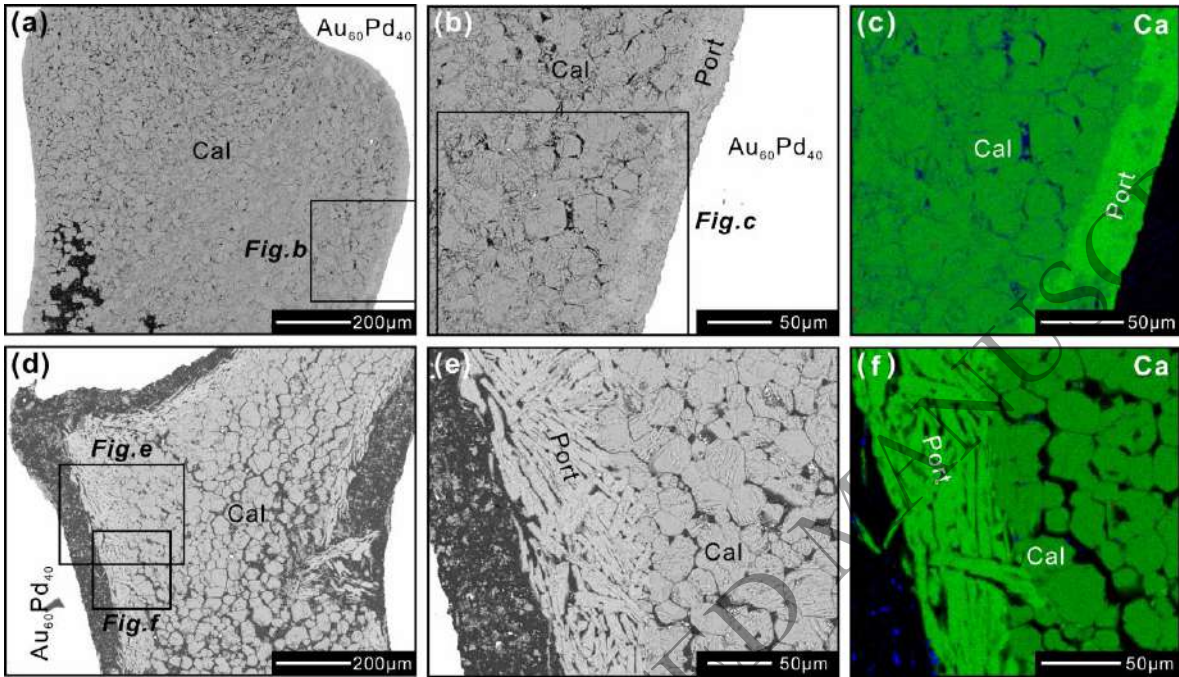


Fig. 2.



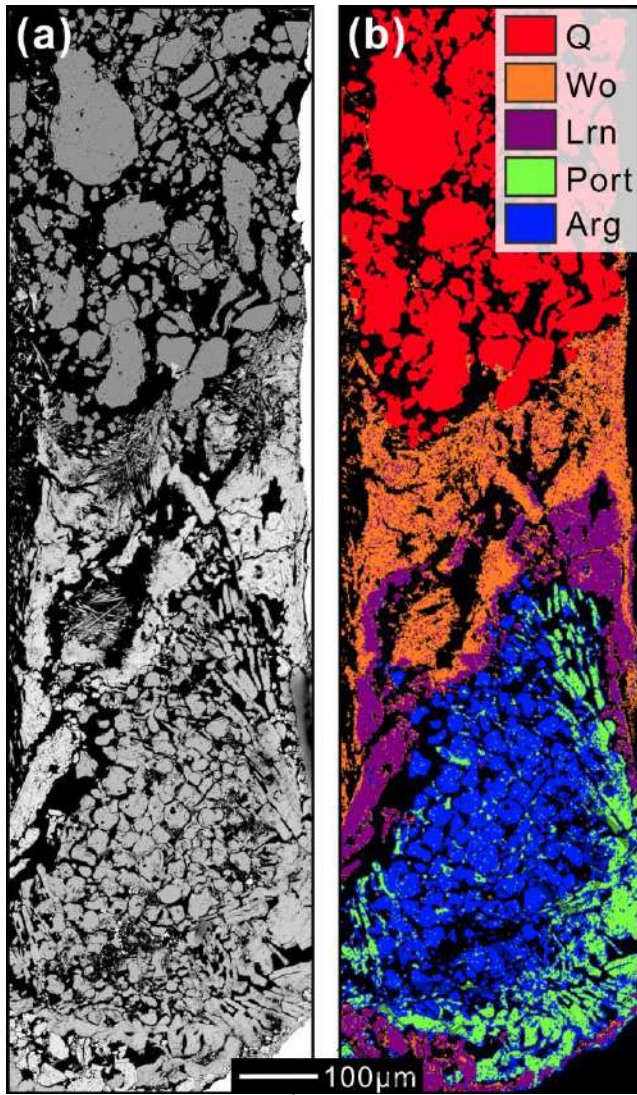
ORIGINAL UNEDITED MANUSCRIPT

Fig. 3.



ORIGINAL UNEDITED MANUSCRIPT

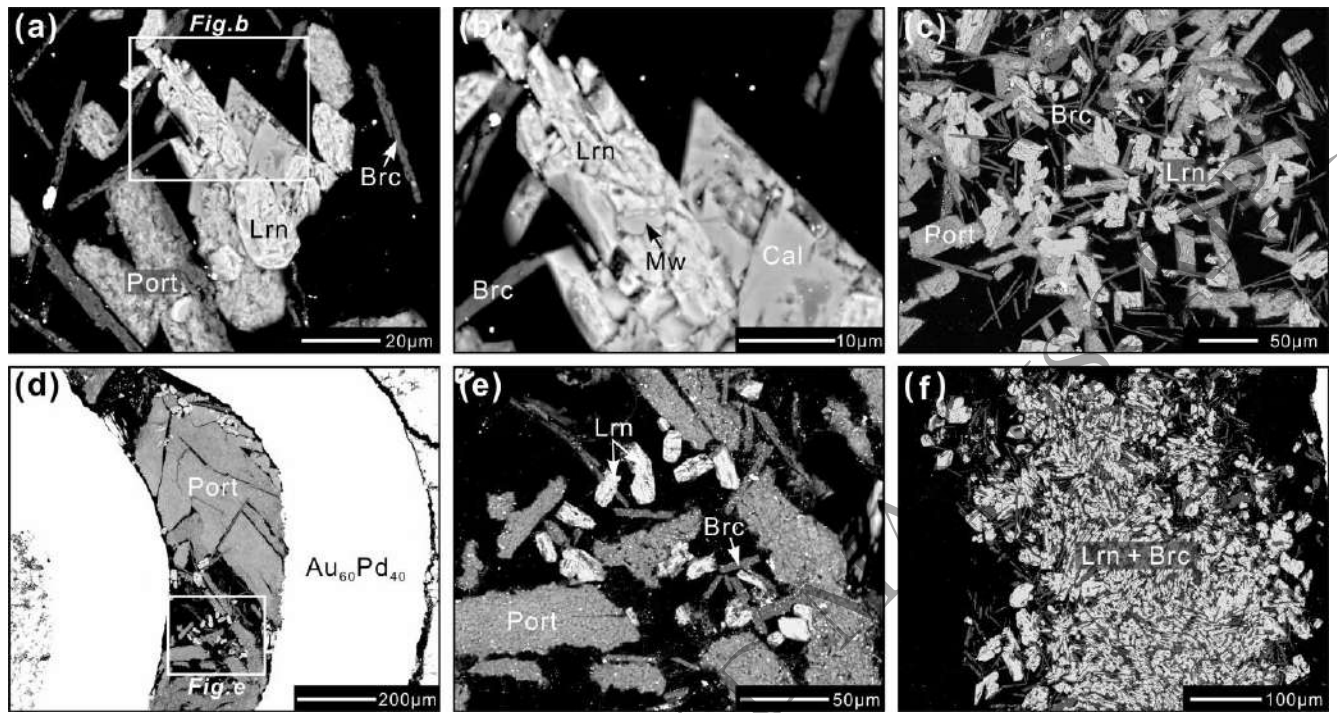
Fig. 4.



ORIGINAL

ACCEPTED MANUSCRIPT

**Fig. 5.**



ORIGINAL UNEDITED

Fig. 6.

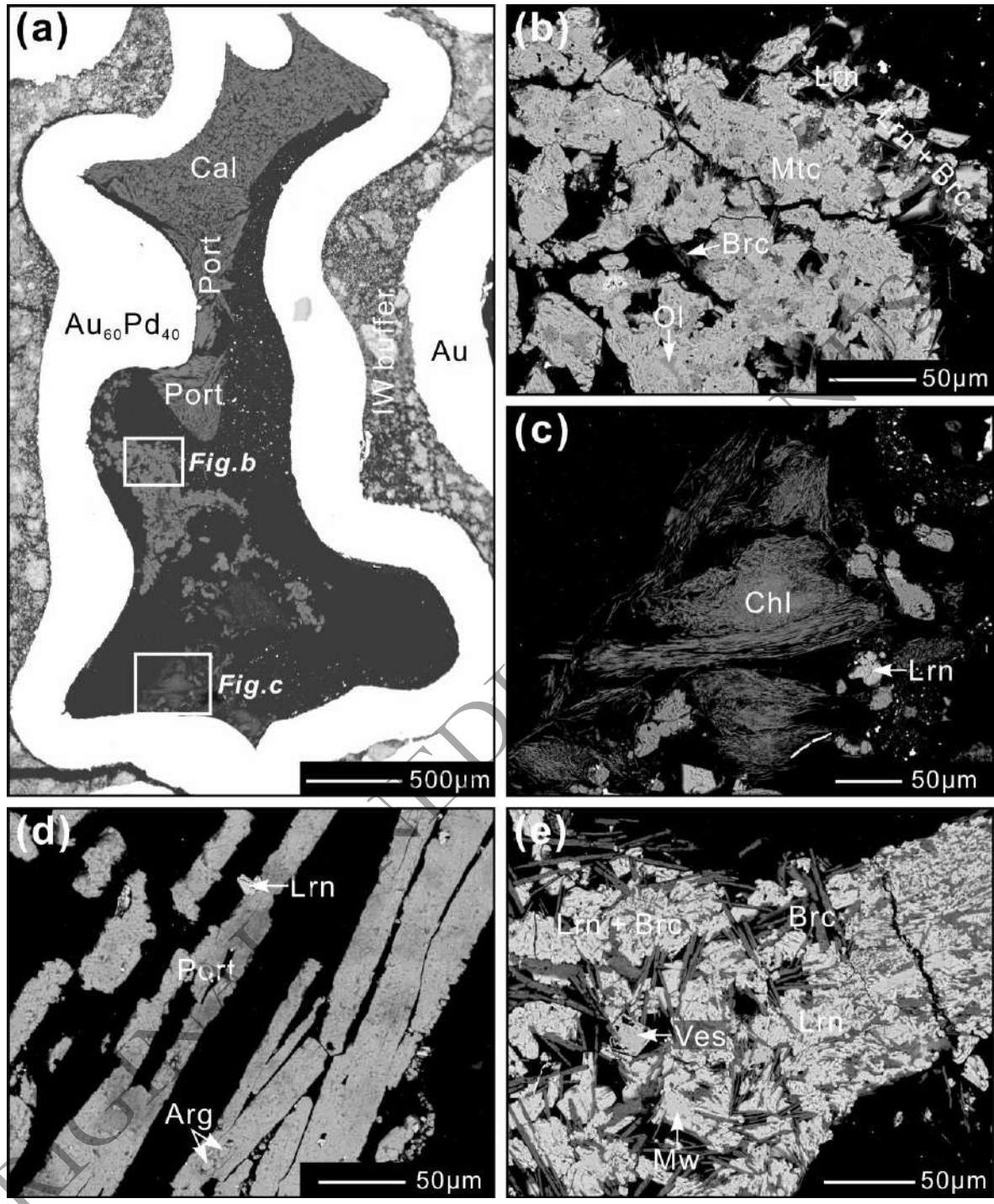


Fig. 7.

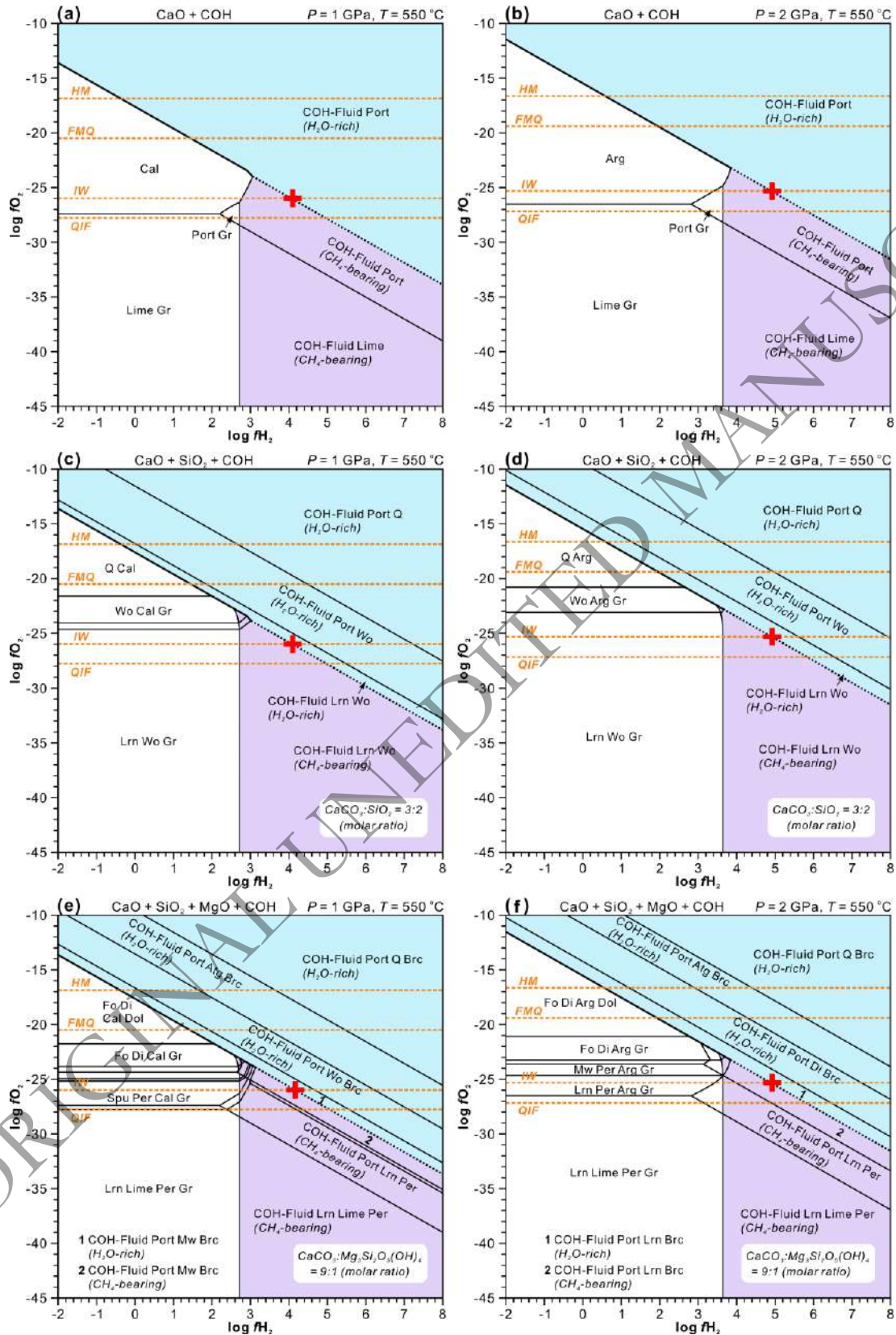


Fig. 8.

1 GPa, 550 °C, F/R = 2, calcite reacting with reduced fluids at initial  $fO_2$  of IW

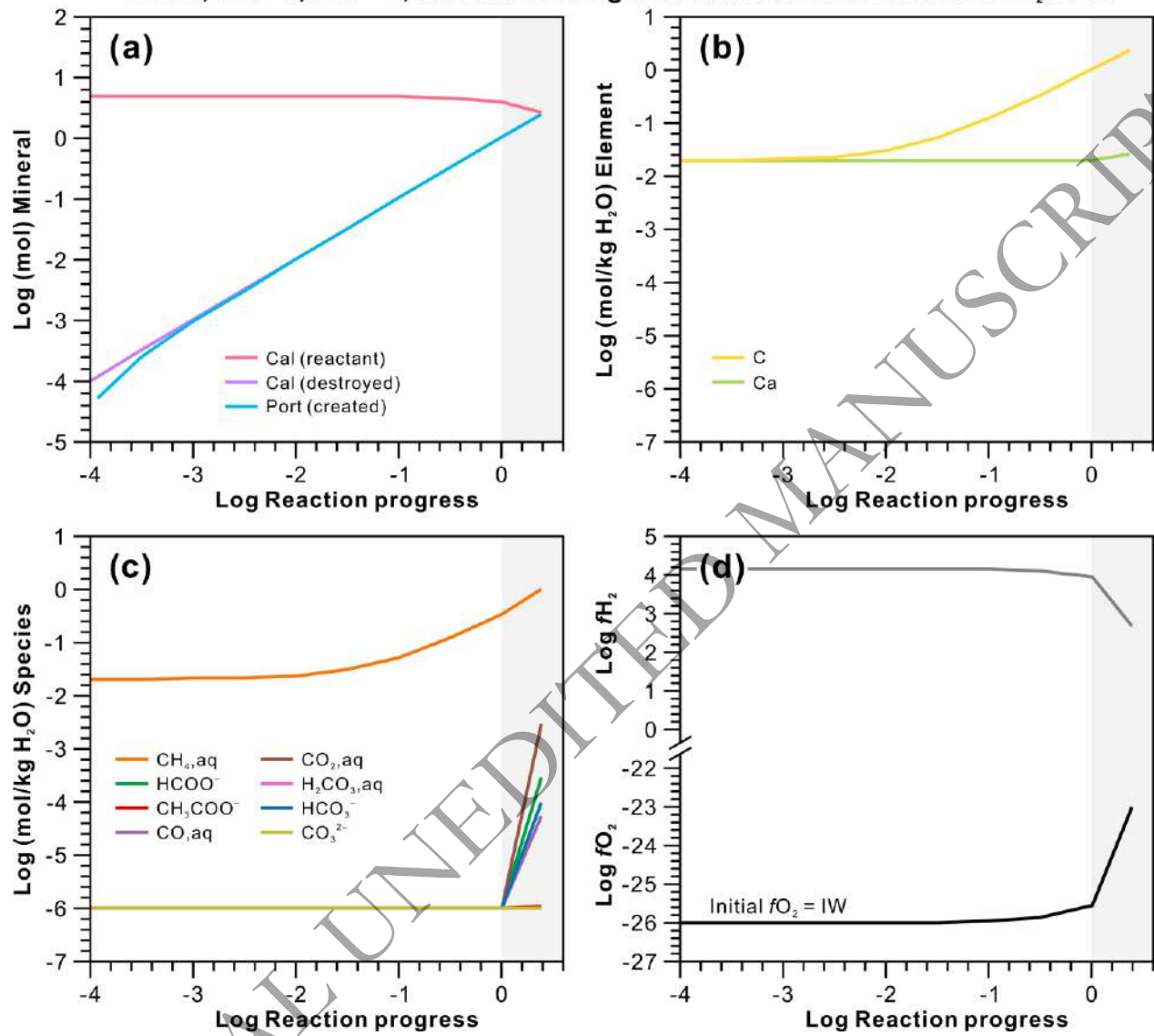
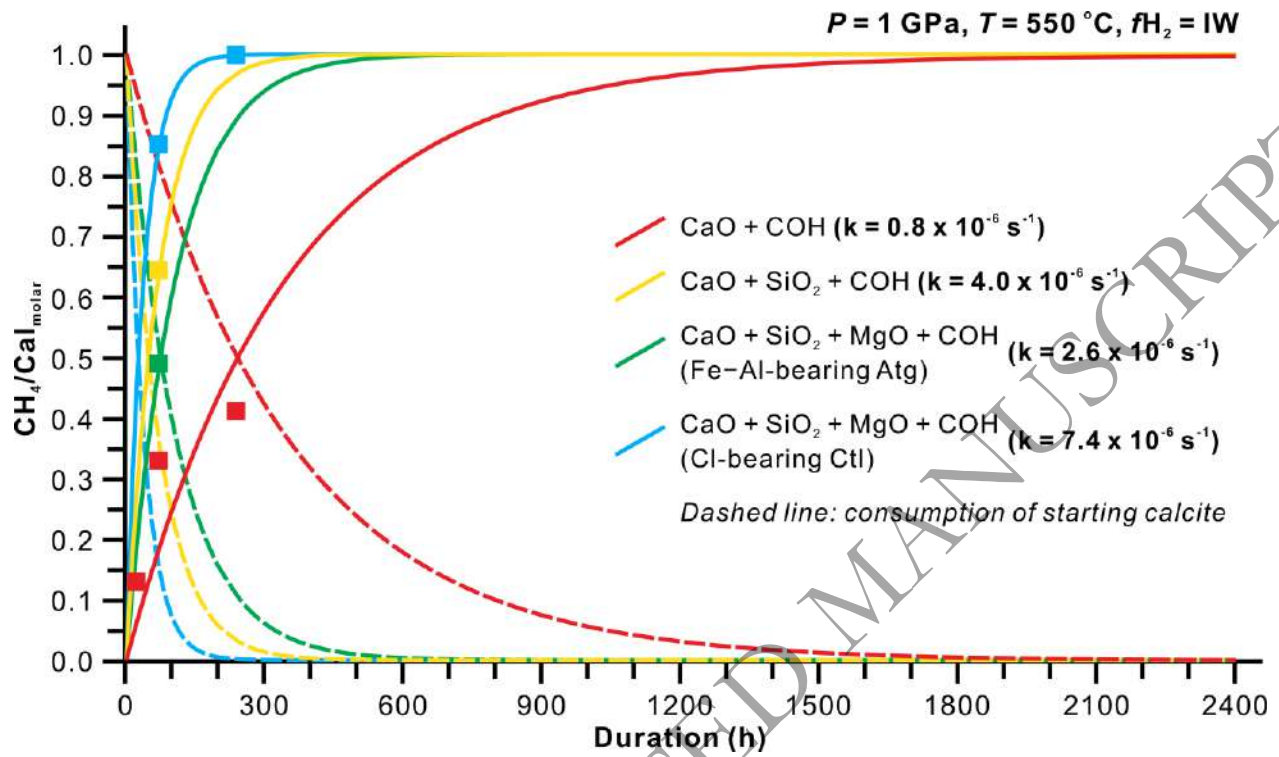


Fig. 9.



ORIGINAL UNEDITED MANUSCRIPT

Fig. 10.

